Ann. Geophys., 41, 147–172, 2023
https://doi.org/10.5194/angeo-41-147-2023

Annales Geophysicae
Open Access
EGU

Ionosonde and GPS total electron content observations during the 26 December 2019 annular solar eclipse over Indonesia

Jiyo Harjosuwito[1], Asnawi Husin[1], Varuliantor Dear[1], Johan Muhamad[1], Agri Faturahman[1], Afrizal Bahar[2], Erlansyah[3], Agung Syetiawan[4], and Rezy Pradipta[5]

[1]Research Center for Space, Research Organization for Aeronautics and Space (LAPAN), National Research and Innovation Agency (BRIN), Bandung, Indonesia
[2]Agam Atmospheric and Space Observation Office, Research Organization for Aeronautics and Space (LAPAN), National Research and Innovation Agency (BRIN), Agam Regency, Indonesia
[3]Pontianak Atmospheric and Space Observation Office, Research Organization for Aeronautics and Space (LAPAN), National Research and Innovation Agency (BRIN), Pontianak, Indonesia
[4]Research Center for Geospatial, Research Organization for Earth Sciences and Maritime, National Research and Innovation Agency (BRIN), Cibinong, Indonesia
[5]Institute for Scientific Research, Boston College, Chestnut Hill, MA, United States

Correspondence: Rezy Pradipta (rezy.pradipta@bc.edu)

Received: 12 September 2022 – Discussion started: 11 October 2022
Revised: 27 January 2023 – Accepted: 10 March 2023 – Published: 13 April 2023

Abstract. We report the investigation of the ionospheric response to the passage of an annular solar eclipse over Southeast Asia on 26 December 2019 using multiple sets of observations. Two ionosondes (one at Kototabang and another at Pontianak) were used to measure dynamical changes in the ionospheric layer during the event. A network of ground-based GPS receiver stations in Indonesia was used to derive the distribution of total electron content (TEC) over the region. In addition, extreme ultraviolet (EUV) images of the Sun from the Atmospheric Imaging Assembly (AIA) instrument on board the Solar Dynamics Observatory (SDO) satellite were also analyzed to determine possible impacts of solar-active regions on the changes that occurred in the ionosphere during the eclipse. We found -1.62 and -1.90 MHz reductions (24.0 % and 27.5 % relative reduction) in *fo*F2 during the solar eclipse over Kototabang and Pontianak, respectively. The respective TEC reductions over Kototabang and Pontianak during the eclipse were -4.34 and -5.45 TECU (24.9 % and 27.9 % relative reduction). Data from both ionosondes indicate a consistent 34–36 min delay between maximum eclipse and minimum *fo*F2. The corresponding time delays for eclipse-related TEC reduction at these two locations were 40 and 16 min, respectively. The ionospheric F layer was found to descend with a speed of 9–19 $\mathrm{m\,s^{-1}}$ during the first half of the eclipse period. We also found an apparent rise in the ionospheric F-layer height near the end of the solar eclipse period, equivalent to a vertical drift velocity of 44–47 $\mathrm{m\,s^{-1}}$. The GPS TEC data mapping along a set of cross-sectional cuts indicates that the greatest TEC reduction actually occurred to the north of the solar-eclipse path, opposite of the direction from which the lunar shadow fell. As the central path of the solar eclipse was located just to the north of the southern equatorial ionization anomaly (EIA) crest, it is suspected that such a peculiar TEC reduction pattern was caused by plasma flow associated with the equatorial fountain effect. Net perturbations of TEC were also computed and analyzed, which revealed the presence of some wavelike fluctuations associated with the solar-eclipse event. Some of the observed TEC perturbation patterns that propagated with a velocity matching the lunar shadow may be explained in terms of nonuniform EUV illumination that arose as various active regions on the Sun went obstructed and unobstructed during the eclipse. The remaining wavelike features are likely to be traveling ionospheric disturbances (TIDs) generated by the passage of the solar eclipse on top of other diurnal factors.

Published by Copernicus Publications on behalf of the European Geosciences Union.

1 Introduction

On 26 December 2019, an annular solar eclipse occurred over the Indonesian sector, specifically over the islands of Sumatra and Kalimantan (Borneo). As an astronomical phenomenon that occurs only a few times a year over varying areas of the globe, any given solar-eclipse event is a unique historical marker that is valuable for investigation from a scientific standpoint. An interesting aspect of solar-eclipse events is their effects on the Earth's atmosphere, including the upper atmosphere or the ionosphere. Research works on the effects of solar eclipses on the Earth's atmosphere started as early as the 1830s (e.g., Birt, 1836; Aplin et al., 2016, and references therein). The effects of solar eclipses on electromagnetic aspects of the ionosphere have been studied since the early 20th century (see Aplin et al., 2016, for an overview). Likewise, studies on the effects of solar eclipses on physical and chemical processes in the ionosphere began around a century ago (Mitra et al., 1933; Beynon, 1955; Ratcliffe, 1956; Rishbeth, 1968, and references therein). Observable effects that solar eclipses might produce on the ionosphere have been quite extensively documented in the peer-reviewed scientific literature (Burton and Boardman, 1933; Cheng et al., 1992; Bamford, 2001; Mansoori et al., 2011; Adekoya et al., 2015). However, any particular solar-eclipse event occurs under its own unique set of background conditions, including geographical location and local solar time. Different solar-eclipse events may produce varying effects on the ionosphere, depending on whether they occur near dawn, around noon, or near dusk (Setty, 1960; Sridharan et al., 2002; St.-Maurice et al., 2011; Chen et al., 2013; Chuo, 2013; Adekoya et al., 2019). Solar-eclipse events that occur over the low-latitude, mid-latitude, and high-latitude regions may also produce different ionospheric effects (Kurkin et al., 2001; Jakowski et al., 2008; Le et al., 2009; Chen et al., 2011; Kumar et al., 2013; Chukwuma and Adekoya, 2016). Likewise, solar-eclipse events that occur during different phases of the 11-year solar cycle may produce different ionospheric effects as well (Adekoya and Chukwuma, 2012).

Initially, scientific investigations on this subject only relied on basic radio observations of the ionosphere (Evans, 1965; Anastassiades, 1970). Nevertheless, data collected from those basic radio observations have yielded important scientific advances (Gledhill, 1959; Price, 1959; Lerfald et al., 1965; Hanuise et al., 1982). Research on this subject can be carried out with ground-based observations (e.g., Choudhary et al., 2011; Atulkar et al., 2015; Frissell et al., 2018; Goncharenko et al., 2018; Liu et al., 2019; Jose et al., 2020) and observations using satellites (e.g., Wang et al., 2010; Cherniak and Zakharenkova, 2018; Hairston et al., 2018). Over time, there have been growing numbers and varying types of ionospheric observation instruments with a wider spatial coverage and geographical distribution. The use of incoherent scatter radars started to become more common in the 1960s (Gordon, 1964; Perkins et al., 1965). A growing network of ground-based global navigation satellite system (GNSS) receivers for total electron content (TEC) measurements became ubiquitous at the turn of the 21st century (Coster et al., 1992; Afraimovich et al., 2002; Rideout and Coster, 2006; Coster et al., 2017; Zhang et al., 2017; Cherniak and Zakharenkova, 2018). Satellite-borne and ground-based optical imaging instruments have also been used for solar-eclipse observations (Eastes et al., 2008; Harding et al., 2018; Aryal et al., 2020; Paulino et al., 2020).

There are still very few well-documented studies on the ionospheric response to solar-eclipse events over the Indonesian sector (Perwitasari and Muslim, 2009; Muslim et al., 2016; Dear and Yulianto, 2016; Vita et al., 2017; Dear et al., 2020). This deficiency is consistent with the shared notion that the Southeast Asian sector is still a relatively understudied area in terms of comprehensively analyzed ionospheric observation data, despite the inherently global and collaborative nature of space research. This regional void has persisted for a long time, in part due to limited space-science knowledge and a lack of ionospheric observation coverage. As such, a comprehensive examination of various ionospheric effects caused by solar-eclipse events, including that on 26 December 2019, is needed – not only scientifically but also institutionally in order to garner a greater level of interest in the region. From a scientific perspective, it is part of ongoing collective efforts from previous research works on this particular subject (Anggarani, 2016; Dear et al., 2020; Faturahman et al., 2022b). From an institutional perspective, it is a timely opportunity to push for a more intensive utilization of existing ionospheric observation instruments in the region as an inclusive part of the global space-science community.

In this paper, we investigated the ionospheric response to the 26 December 2019 annular solar-eclipse event over the Indonesian sector using a combination of ionosonde and GNSS receiver observations, in conjunction with solar-image analysis. The present work adds to existing analyses of this particular event performed independently by Aa et al. (2020) and Barad et al. (2022) over the Indian and Southeast Asian longitudes. Specifically, the present work reveals greater spatiotemporal details of ionospheric changes that occurred over the western part of Indonesia due to the eclipse. Section 2 of this paper describes the methodology, Sect. 3 describes the results, Sect. 4 presents the discussion of the findings, and Sect. 5 presents the conclusion.

2 Instruments and methodology

Recently, there have been some notable changes in terms of ionospheric observation instruments within the Indonesian sector. In the last 2 decades or so, a network of ground-based GNSS receiver stations in the region has been growing steadily (Masykur, 2021), which may provide adequate TEC data coverage. In Indonesia, those GNSS receiver stations

are part of a larger infrastructure managed by the Geospatial Information Agency (Badan Informasi Geospasial – BIG), the primary purpose of which is geodetic surveying. These GNSS receivers complement the existing ionosondes, which had been the dominant type of ionospheric observation instruments in Southeast Asia since the 1950s (Sen, 1949; Osborne, 1951; Minnis, 1957) and in Indonesia since the 1980s (Haggard, 1985, 1988; Gage et al., 1989; Lynn et al., 2000, 2004). In addition, there is also the Equatorial Atmosphere Radar (EAR) facility in Kototabang, West Sumatra, which is a collaboration between the Indonesian Space Agency (LAPAN) and Kyoto University, Japan (Fukao et al., 2003). The current coverage of ionospheric observation instruments in Indonesia is still incomplete, especially in the eastern territory, where observation instruments remain relatively rare. Perhaps it will take another decade until a more complete observation coverage is finally realized. Nevertheless, the distribution of existing instruments is more than sufficient to support many ionospheric research activities, including our examination of the 26 December 2019 annular solar-eclipse event (present paper). Figure 1 shows the spatial distribution of available instruments during the solar-eclipse event in relation to the main eclipse trajectory.

This study used observation data from ionosondes and the GNSS receiver network in the Indonesian sector. A separate analysis of the EAR Kototabang observation data during this solar-eclipse event is published elsewhere (Faturahman et al., 2022a). In addition, analysis of masked solar images was also performed to quantify the degree of inhomogeneity in the solar EUV illumination during the eclipse.

2.1 Ionosonde measurements

The ionosondes used for this study are located in Kototabang, West Sumatra (0.20° S, 100.32° E), and Pontianak, West Kalimantan (0.02° S, 109.33° E). For the 26 December 2019 annular solar eclipse, the maximum solar obscuration at these two locations (cf. Fig. 1) ranges between 91 % and 94 %. From 1 d prior to the eclipse event until 1 d after the eclipse event, ionosondes at these two stations were set to record one ionogram every 5 min. On other days, ionograms were recorded once every 15 min.

At the Kototabang station, a frequency-modulated continuous-wave (FMCW) ionosonde owned by the Japanese National Institute of Information and Communications Technology (NICT) was in operation. Meanwhile, at the Pontianak station, a Canadian Advanced Digital Ionosonde (CADI) owned by the Indonesian National Institute of Aeronautics and Space (LAPAN) was in operation. Both ionosondes have been in continuous operation since 2004, and they were in the midst of some repair and maintenance work during the 26 December 2019 annular solar-eclipse event. As a result, the noise level in the recorded ionograms was high, which necessitated a manual scaling process for the ionogram data analysis and interpretation. Figure 2 shows sample ionograms that were recorded at these two stations during the solar-eclipse event.

Manual scaling of ionospheric parameters from the ionograms was performed based on standard procedures provided in the UAG-23A handbook (Piggott and Rawer, 1972). Essential ionospheric parameters that were derived through ionogram scaling include the critical frequency of the F1 layer (*fo*F1), critical frequency of the F2 layer (*fo*F2), and apparent parabolic-layer peak height (*hp*F2). The scaling process was performed for all ionograms recorded in December 2019.

2.2 Ground-based GPS TEC measurements

Dual-frequency GNSS receiver data can be used to derive TEC along the line of sight. The theory and algorithm for calculating TEC from GNSS data are based on the refractive properties of the ionospheric layer as a function of the frequency of the GNSS signal. For a given frequency f, the time delay τ along the GPS signal path is inversely proportional to the GPS signal carrier frequency as $\tau = 40.3\,\mathrm{TEC}/(cf^2)$, where c is the speed of light (Klobuchar, 1996). From the two frequencies f_1 and f_2, we have a differential time delay of $\Delta\tau = \tau_2 - \tau_1$, from which the TEC value can be obtained using the following equation:

$$\Delta\tau = \frac{40.3}{c}\frac{\mathrm{TEC}}{\frac{1}{f_2^2}-\frac{1}{f_1^2}}. \tag{1}$$

This equation can be rewritten in terms of slant TEC (STEC) and the pseudorange P as

$$\mathrm{STEC_p} = \frac{f_1^2(P_1 - P_2) - \mathrm{bs} - \mathrm{Br}}{40.3(1-\gamma^2)} \tag{2}$$

or in terms of STEC and the carrier phase ϕ as

$$\mathrm{STEC}_\phi = \frac{f_1^2(\lambda_1\phi_1 - \lambda_2\phi_2) - (\lambda_1 N_1 - \lambda_2 N_2) - \mathrm{bs} - \mathrm{Br}}{40.3(1-\gamma^2)}, \tag{3}$$

where bs is the satellite bias, Br is the receiver bias, and $\lambda_{1,2} = c/f_{1,2}$, $\gamma = f_1/f_2$, and $N_{1,2}$ are integers. STEC measurements from pseudoranges produce TEC values with high noise levels, while those from carrier phases produce more precise TEC values, albeit with ambiguity. Mannucci et al. (1993) and Skone (1998) provided a way to combine the two measurements to produce a precise TEC without the ambiguity. It is also necessary to convert STEC to the equivalent vertical TEC (VTEC), which can be written as

$$\mathrm{VTEC} = M(\theta)\cdot\mathrm{STEC},$$
$$\text{with } M(\theta) = \sqrt{1 - \left(\frac{R_\mathrm{E}}{R_\mathrm{E}+h}\right)^2 \sin^2\theta}, \tag{4}$$

where R_E is the Earth's radius, h is the height of the ionospheric shell, and θ is the zenith angle.

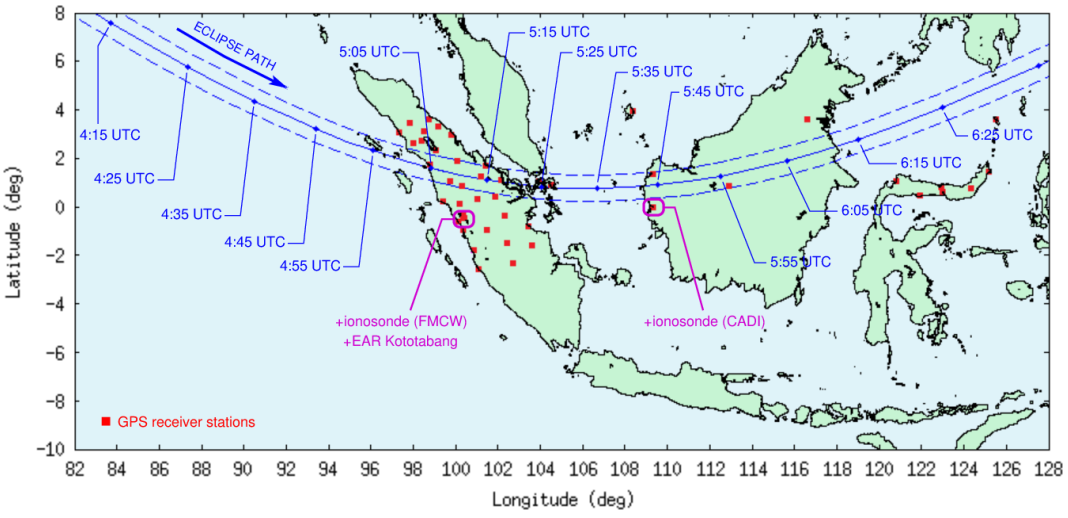

Figure 1. Geographical map showing the path of the 26 December 2019 annular solar eclipse over Southeast Asia as well as a suite of ground-based radio diagnostic instruments used in the study.

We derived the regional TEC using GNSS observation data in receiver-independent-exchange (RINEX) format from the Indonesian Continuously Operating Reference Station (INACORS) network, which is maintained by the Indonesian Geospatial Information Agency (BIG). The observation data are catalogued at http://inacors.big.go.id/sbc/ (last access: 4 April 2023) by the BIG. In 2019, the INACORS network consisted of 207 receiver stations. In this study, we used data from 46 receiver stations that are distributed in Sumatra and Kalimantan (cf. Fig. 1). Geographic coordinates of the INACORS stations that we used in this study are provided in the Supplement. The number of GNSS receiver stations in Sumatra is greater than that in Kalimantan, since the INACORS network is used primarily for geodetic mapping and monitoring of the Eurasian tectonic plate.

The TEC values were calculated from the RINEX observation files using the Gopi data-analysis software (Rama Rao et al., 2006; Seemala and Valladares, 2011). Only signals from the GPS constellation were used in the TEC computation, and the elevation angle cutoff was set at 20°. For the purpose of spatial mapping of TEC data in this study, we selected an altitude of 350 km for the ionospheric piercing points (IPPs). Figure 3a–c show sample snapshots of TEC observations obtained from basic processing of the data, illustrating the spatial coverage provided by these receiver stations. Observations at 05:30 UTC on 25, 26, and 27 December 2019 are shown in these snapshots, with the IPPs represented as open circles and the TEC values indicated using a color map. The solar-eclipse path on 26 December 2019 is shown as a dashed blue curve, and the instantaneous position of the lunar shadow at that time is indicated by a solid gray circle. A significant decrease in TEC values around the eclipse path on 26 December 2019 is quite visible on the data map. An animated version of Fig. 3a–c is also provided in the Supplement.

As part of the analysis, TEC data detrending was also performed. Two types of data detrending were performed, (1) to derive ΔTEC (general deviations from the normal condition) and (2) to derive TEC perturbation (TECP) (wavelike perturbations with much smaller amplitudes and finer structures). The derivation of ΔTEC was performed on TEC values that had been spatially mapped from individual IPPs onto fixed grid point(s). The baseline for detrending the TEC data into ΔTEC was based on the average diurnal TEC variation from calendar dates other than the solar-eclipse day. In contrast, the derivation of TECP was performed using TEC time series on the individual IPPs. The baseline for detrending the TEC data into TECP was obtained via a 30 min running average of the TEC time series being examined. After the TEC detrending process along the IPP trajectory was completed, the resulting TECP values were spatially mapped onto fixed grid points.

In addition, we also used the keogram technique to analyze detailed spatiotemporal variations of TEC, ΔTEC, and TECP data. A keogram was traditionally defined as a plot with latitude on the y-axis, time on the x-axis, and a color scale to represent the intensity of auroral emission (Eather et al., 1976). In the present paper, we use a broader definition of keograms: data plots with a geographic dimension (latitude or longitude) on one axis and time on the other axis, showing a certain physical quantity (e.g., TEC) with a color-scale representation. Keograms had been used widely in ionospheric data analysis. For example, Wang et al. (2020) used TEC keograms to analyze the dynamics of large-scale irregularities in the polar ionosphere. Coster et al. (2017) used a keogram of differential TEC to show the appearance of ionospheric disturbances during the 21 August 2017 solar

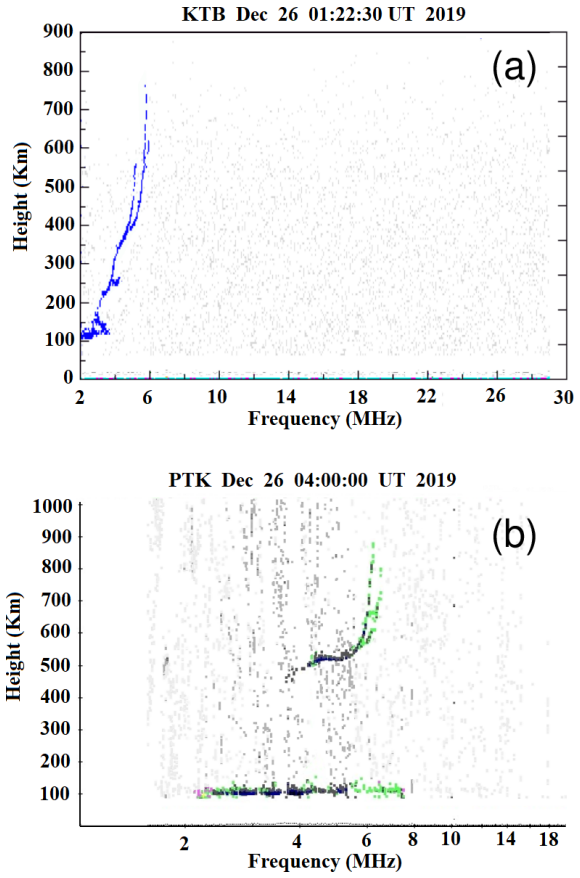

Figure 2. Sample ionograms from **(a)** Kototabang station at 01:22 UTC on 26 December 2019 and **(b)** Pontianak station at 12:00 LT (05:00 UTC) on 26 December 2019. Main return traces in these sample ionograms have been enhanced to make them stand out against high levels of background noise. Ionograms from these two stations were subject to a manual scaling process in order to extract essential ionospheric parameters.

eclipse over North America. In order to construct keogram plots of TEC, ΔTEC, and TECP data, we defined a few cross-sectional cut lines along and perpendicular to the eclipse trajectory. The TEC, ΔTEC, and TECP data are then spatially mapped/projected onto the defined cut lines, and the cut line-projected data at various epochs were stacked sequentially to form the keograms. Figure 3d shows an example keogram of TEC values at longitude 104° E on 25 December 2019.

2.3 Solar EUV illumination calculation

We investigated changes in EUV radiation that illuminated various points in the Earth's upper atmosphere during the eclipse. For computational purposes, the solar EUV illumination was considered at 100 km altitude above the Earth's surface. EUV images of the Sun were obtained from the Atmospheric Imaging Assembly (AIA) instrument on board the Solar Dynamics Observatory (SDO) satellite to represent the solar EUV emissions from the corona. We used an AIA 193 Å image taken at 03:10:04 UTC on 26 December 2019 as the representative solar-disk image. Because there was no solar flare activity recorded during the eclipse, we assumed that there was no significant change on the Sun's surface, and therefore a single sample image was sufficient to represent the Sun at all times during the eclipse event. Although there was no solar flare at that time, there were two active regions (ARs) on the Sun with higher levels of emission: one in the southeast of the solar disk and the other in the northwest of the solar disk.

We have implemented a computer model of a solar eclipse that can reproduce the obscuration of the Sun as viewed from any point on Earth. The EUV image of the Sun was placed at the center of the field of view of the simulation, and a model of the Moon was moved across the Sun based on the DE421 ephemeris data developed by the Jet Propulsion Laboratory, NASA. We used the Skyfield library in the Python programming language to develop the simulation and plotted the sequential motion of the artificial Moon with a 1 min time cadence to represent the eclipse. Changes in the EUV radiation received on Earth during the eclipse can be approximated as the change in total intensities of all pixels in the image, with some of the pixels blocked by the artificial Moon. This is based on an approach previously performed by Huba and Drob (2017).

Figure 4 illustrates this modeling of solar EUV illumination during the eclipse. Here we calculated the time evolution of solar illuminance and EUV 193 Å irradiance received at the lower ionosphere (at 100 km altitude) over a geographic site near the greatest eclipse point in Siak (1.01° N, 102.25° E), Indonesia. In order to enhance the eclipse effect on the solar EUV radiation received on Earth, we changed the contrast of the image. This was done to emphasize the presence of ARs on the Sun by darkening the low-intensity regions and intensifying the bright regions, such as the ARs. An emphasis on ARs is needed because ARs are small concentrated areas with high brightness, which would abruptly disappear as the solar obscuration gradually changes. By performing this procedure, variation in the solar EUV radiation (i.e., the EUV obscuration factor) during the eclipse can become more obvious, as shown by the purple line in the time series plot.

Further, at various epochs during the eclipse, we also computed the total solar EUV irradiance over a number of evenly spaced grid points within a rectangular region from latitude 12° S to 7° N and from longitude 90 to 150° E with 1° spatial resolution. At any given epoch, spatial nonuniformity of the solar EUV irradiance can then be quantified. We followed the approach by Huba and Drob (2017) and Mrak et al. (2018) to identify this nonuniformity by calculating the second spatial derivative (i.e., the Laplacian) of the distribution of solar EUV radiation received on Earth. This is a reasonable approach, as the Laplacian has been frequently used in image processing for edge detection (e.g., Wang, 2007). The Laplacian operator can be applied to enhance features in an

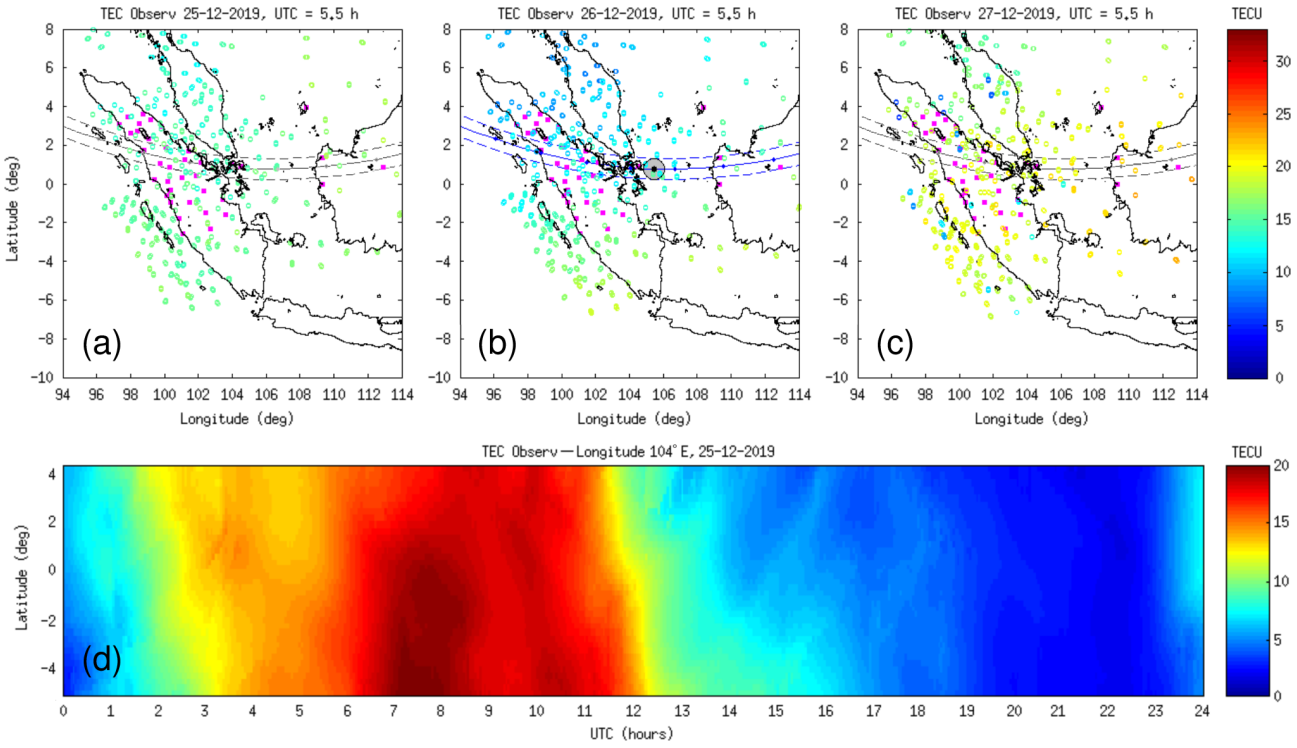

Figure 3. Geographical maps showing the spatial distribution of the GPS IPPs at 350 km altitude at 05:30 UTC on **(a)** 25, **(b)** 26, and **(c)** 27 December 2019. The path of the annular solar eclipse on 26 December 2019 is shown as a blue curve, and the location of eclipse annularity at this epoch is shown as a gray-filled circle. As a visual guide, the eclipse path is also displayed as a gray curve on 25 and 27 December 2019. Locations of ground-based GPS receiver stations are shown as magenta squares, and the TEC observation values are indicated on the individual IPPs using a color map. **(d)** Sample TEC keogram on 25 December 2019.

image that has sharp discontinuity or rapid change in intensity (Gonzalez and Woods, 2018). The main advantage of the Laplacian operator is its low computational cost. In addition, the Laplacian operator is isotropic, which simplifies the interpretation of results. On the other hand, a Laplacian operator does not provide the edge direction, which is its disadvantage (Nixon and Aguado, 2002). Nevertheless, edge direction is not very important in our situation, and our analysis was not adversely impacted.

3 Observation results

In this section, we present the results that were obtained from the ground-based radio observation instruments (ionosondes and GNSS receivers) and those from the solar EUV illumination analysis.

3.1 Ionosonde observations

Results from ionosonde observations and manual scalings of the recorded ionograms are presented here in terms of *fo*F2, *fo*F1, and *hp*F2 variations. In order to provide additional contexts, the corresponding relations to *Nm*F2, *Nm*F1, and apparent vertical drift velocity are also presented.

Figure 5 shows the time series plots of *fo*F2 over Kototabang and Pontianak on 26 December 2019. Based on the ionosonde observations, changes in *fo*F2 as a response to the solar eclipse were generally found to exhibit two distinct phases: a reduction phase and a recovery phase.

Over Kototabang, a reduction in *fo*F2 was seen starting at 04:35 UTC (11:35 LT) from an initial value of 6.70 MHz ($NmF2 \approx 5.54 \times 10^5$ el cm^{-3}) to reach its minimum value of 5.50 MHz ($NmF2 \approx 3.73 \times 10^5$ el cm^{-3}) at 05:45 UTC (12:45 LT). During the 70 min of this reduction phase, *fo*F2 dropped by 1.20 MHz. This *fo*F2 reduction is equivalent to a drop in *Nm*F2 by 1.81×10^5 el cm^{-3}, which gives us an average rate of ionospheric-density reduction of -43 el cm^{-3} s^{-1}. The recovery phase started at 05:45 UTC (12:45 LT) and ended at 08:45 UTC (15:45 LT) with an increase in *fo*F2 by 1.60 MHz, from 5.50 to finally reach 7.10 MHz ($NmF2 \approx 6.22 \times 10^5$ el cm^{-3}) over a 180 min duration. This is equivalent to a rise in *Nm*F2 by 2.49×10^5 el cm^{-3} during the recovery phase, which gives us an average rate of ionospheric-density increase of $+23$ el cm^{-3} s^{-1}.

Meanwhile, over Pontianak, a reduction in *fo*F2 started at 04:50 UTC (11:50 LT) from an initial value of 6.21 MHz ($NmF2 \approx 4.76 \times 10^5$ el cm^{-3}) to reach its minimum value of 5.44 MHz ($NmF2 \approx 3.65 \times 10^5$ el cm^{-3}) at 06:20 UTC

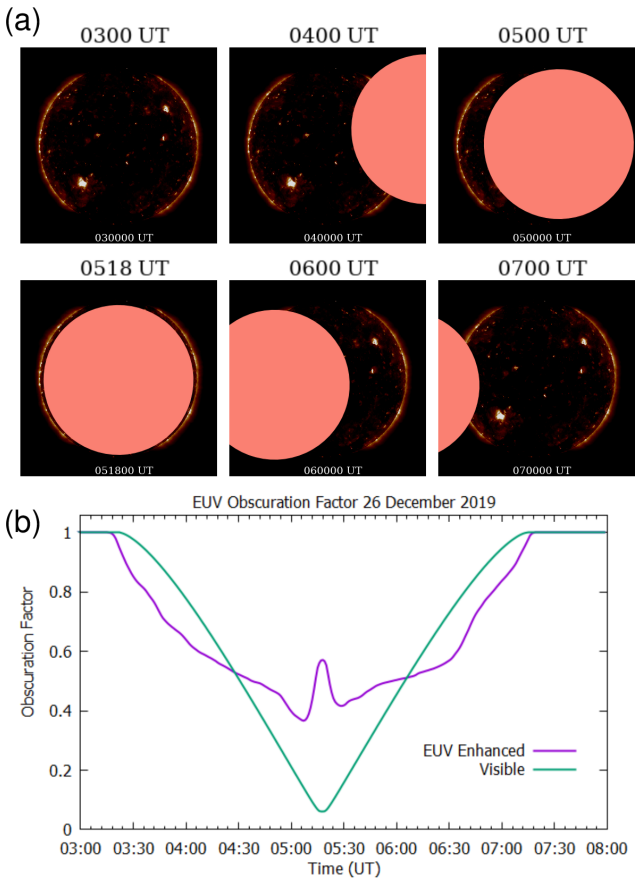

Figure 4. **(a)** Sample sequence of digitally masked 193 Å (19.3 nm) solar AIA images on 26 December 2019 to estimate the level of solar obscuration at a given point on the Earth's surface during the course of the solar eclipse. **(b)** Time series variation of the obscuration of solar irradiance at various wavelengths during the 26 December 2019 annular solar eclipse over Siak, Riau province (1.01° N, 102.25° E), calculated using this computational masking method.

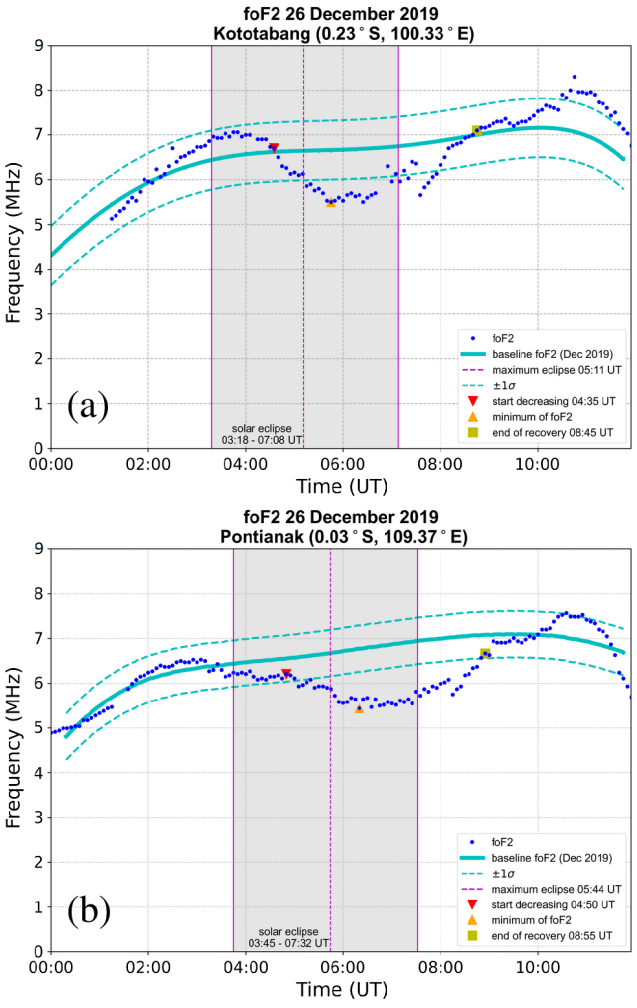

Figure 5. Time series plots of ionospheric F2-layer critical frequencies (*fo*F2) from scaling of ionosonde measurements at **(a)** Kototabang and **(b)** Pontianak on 26 December 2019. Observation data are shown in blue, the baseline *fo*F2 level based on December 2019 averages is shown as cyan curves, and the solar eclipse period is indicated with gray bands.

(13:20 LT). During the 90 min of this reduction phase, *fo*F2 dropped by 0.77 MHz. This *fo*F2 reduction is equivalent to a drop in *Nm*F2 by 1.11×10^5 el cm^{-3}, which gives us an average rate of ionospheric-density reduction of -20.6 el cm^{-3} s^{-1}. The recovery phase occurred over a duration of 155 min, starting at 06:20 UTC (13:20 LT) until 08:55 UTC (15:55 LT), with an increase in *fo*F2 by 1.23 MHz (from 5.44 to 6.67 MHz). This is equivalent to a rise in *Nm*F2 by 1.84×10^5 el cm^{-3} during the recovery phase, which gives us an average rate of ionospheric-density recovery of $+19.9$ el cm^{-3} s^{-1}.

Observations over Kototabang and Pontianak indicate that there was some lag between the start of the eclipse and the initial decrease in *fo*F2. Over Kototabang, there was a time lag of 77 min before *fo*F2 started to decrease, while the corresponding time lag over Pontianak was around 65 min. Likewise, the recovery phase extended well beyond the end of the eclipse. The extra time between the end of the eclipse and the end of the recovery phase over Kototabang was 97 min, whereas that over Pontianak was 83 min.

With respect to the normal baseline (derived based on averaging and smoothing of ionosonde observations from other days in December 2019), the magnitude of *fo*F2 reduction over Kototabang and Pontianak was quite similar. The reduction in *fo*F2 over Kototabang with respect to the normal baseline was -1.62 MHz (a 24.0 % relative reduction); meanwhile, that over Pontianak was -1.90 MHz (a 27.5 % relative reduction).

Figure 6 shows the time series plots of *fo*F1 over Kototabang and Pontianak on 26 December 2019. Similar to what we have observed for *fo*F2, changes in the critical frequency of the ionospheric F1 layer as a response to the solar eclipse

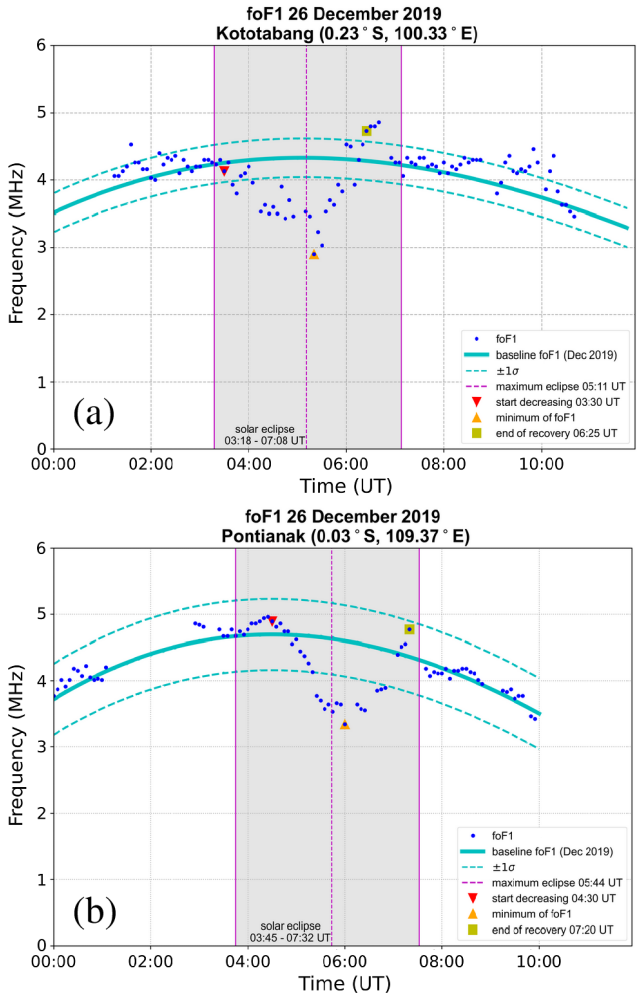

Figure 6. Time series plots of ionospheric F1-layer critical frequencies (*fo*F1) from scaling of ionosonde measurements at **(a)** Kototabang and **(b)** Pontianak on 26 December 2019. Observation data are shown in blue, the baseline *fo*F1 level based on December 2019 averages is shown as cyan curves, and the solar eclipse period is indicated with gray bands.

also exhibited two distinct phases: a reduction phase and a recovery phase.

Over Kototabang, reduction in *fo*F1 started at 03:30 UTC (10:30 LT), which was 12 min after the start of the eclipse, with an initial *fo*F1 of 4.13 MHz which corresponds to an *Nm*F1 of 2.11×10^5 el cm^{-3}. The minimum *fo*F1 of 2.9 MHz (*Nm*F1 $\approx 1.04 \times 10^5$ el cm^{-3}) was reached at 05:20 UTC (12:20 LT), which was 9 min after the maximum eclipse. Afterwards, *fo*F1 started its recovery phase to finally reach 4.73 MHz (*Nm*F1 $\approx 2.76 \times 10^5$ el cm^{-3}) at 06:25 UTC (13:25 LT), which was 43 min before the end of the eclipse.

The duration of the reduction phase was 110 min, in which *fo*F1 dropped by 1.23 MHz (from 4.13 to 2.90 MHz). This *fo*F1 reduction corresponds to a drop in ionospheric density by 1.07×10^5 el cm^{-3} (from 2.11×10^5 to 1.04×10^5 el cm^{-3}). This gives an average rate of ionospheric-density reduction of -16 el cm^{-3} s^{-1}. With respect to the normal baseline value of 4.33 MHz, the minimum *fo*F1 was 1.43 MHz lower (a 33 % relative reduction). The recovery phase occurred over a duration of 65 min, with an increase in *fo*F1 by 1.83 MHz (Δ*Nm*F1 $\approx 1.72 \times 10^5$ el cm^{-3}), which gives us an average rate of ionospheric-density recovery of $+44$ el cm^{-3} s^{-1}.

Meanwhile, over Pontianak, observations indicate that *fo*F1 started to decrease at 04:30 UTC (11:30 LT), which was 45 min after the start of the eclipse, with an initial *fo*F1 of 4.89 MHz (*Nm*F1 $\approx 2.97 \times 10^5$ el cm^{-3}). The minimum *fo*F1 of 3.34 MHz (*Nm*F1 $\approx 1.38 \times 10^5$ el cm^{-3}) was reached at 06:00 UTC (13:00 LT), which was 16 min after the maximum eclipse. Afterwards, *fo*F1 started its recovery phase to finally reach 4.77 MHz (*Nm*F1 $\approx 2.83 \times 10^5$ el cm^{-3}) at 07:20 UTC (14:20 LT), which was 12 min before the end of the eclipse.

The *fo*F1 reduction phase over Pontianak took place over a 90 min duration, in which *fo*F1 dropped by 1.55 MHz (from 4.89 to 3.34 MHz). This *fo*F1 reduction corresponds to a drop in *Nm*F1 by 1.59×10^5 el cm^{-3} (from 2.97×10^5 to 1.38×10^5 el cm^{-3}). This gives an average rate of ionospheric-density reduction of -29 el cm^{-3} s^{-1}. With respect to the normal baseline value of 4.58 MHz, the minimum *fo*F1 was 1.24 MHz lower (a 27 % relative reduction). The recovery phase occurred over a duration of 80 min, with an increase in *fo*F1 by 1.43 MHz (from 3.34 to 4.47 MHz). This rise in *fo*F1 corresponds to an increase in *Nm*F1 by 1.43×10^5 el cm^{-3} (from 1.38×10^5 to 2.83×10^5 el cm^{-3}). This gives us an average rate of ionospheric-density recovery of $+30$ el cm^{-3} s^{-1}.

Figure 7 shows the time series plots of *hp*F2 measurements at Kototabang and Pontianak on 26 December 2019. Based on these observations, changes in *hp*F2 as a response to the solar eclipse can be categorized into three phases: a descending phase, a rising phase, and a recovery phase.

The ionospheric response over Kototabang in terms of *hp*F2 is shown in Fig. 7a. During the first phase that started at 03:20 UTC (10:20 LT), which was 12 min after the start of the eclipse, *hp*F2 descended from an initial altitude of 516 km. The descent occurred for a 95 min duration until 04:55 UTC (11:55 LT), when *hp*F2 reached an altitude of 466 km. With *hp*F2 descending by 50 km, the average rate of descent during this first phase was approximately -32 km h^{-1} or -8.8 m s^{-1}. At 05:30 UTC (12:30 LT), *hp*F2 started to rise from an altitude of 486 km to reach 682 km at 06:40 UTC (13:40 LT). With *hp*F2 rising by 196 km during this second phase, the average rate of ascent was 168 km h^{-1} or 47 m s^{-1}. The recovery phase subsequently occurred over a 20 min duration, ending at 07:00 UTC (14:00 LT), when *hp*F2 returned to the baseline level.

The ionospheric response over Pontianak in terms of *hp*F2 is shown in Fig. 7b. The first phase started at 03:55 UTC (10:55 LT), which was 10 min after the start of the eclipse, with an initial *hp*F2 of 616 km. This phase occurred over a 120 min duration until 05:55 UTC (12:55 LT), when *hp*F2 reached an altitude of 480 km. In other words, *hp*F2 de-

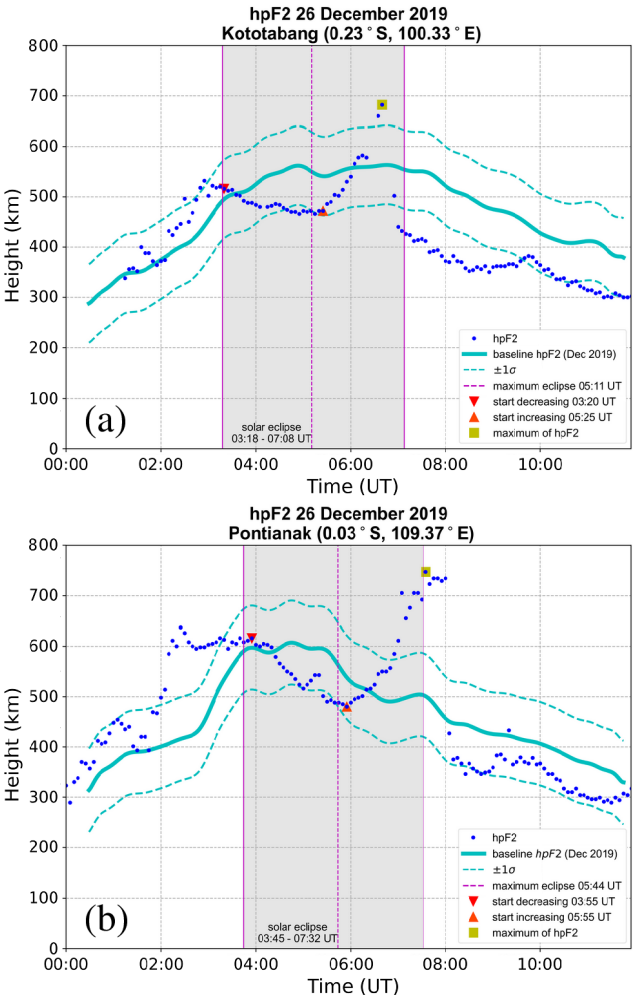

Figure 7. Time series plots of ionospheric height with maximum electron density (*hp*F2) from scaling of ionosonde measurements at **(a)** Kototabang and **(b)** Pontianak on 26 December 2019. Observation data are shown in blue, the baseline *hp*F2 level based on December 2019 averages is shown as cyan curves, and the solar eclipse period is indicated with gray bands.

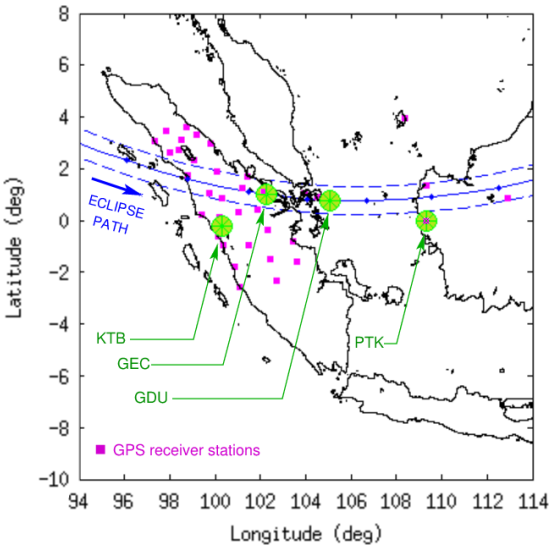

Figure 8. Geographical map showing a set of discrete checkpoints for the TEC and ΔTEC time series analysis shown in Figs. 9 and 10. These fixed checkpoints are over Kototabang (KTB; 0.20° S, 100.32° E), the point of greatest eclipse (GEC; 1.01° N, 102.25° E), the point of greatest annularity duration (GDU; 0.78° N, 105.08° E), and Pontianak (PTK; 0.04° S, 109.35° E). The path of the annular solar eclipse is shown on the map as a blue curve and locations of ground-based GPS receiver stations as magenta squares.

scended by 136 km, which means that the average rate of descent was $-68\,\mathrm{km\,h^{-1}}$ or $-19\,\mathrm{m\,s^{-1}}$. The second phase occurred for a 100 min duration, starting from 05:55 UTC (12:55 LT) until 07:35 UTC (14:35 LT), during which *hp*F2 rose from 480 to 747 km. With *hp*F2 rising by 267 km, the average rate of ascent was $160\,\mathrm{km\,h^{-1}}$ or $44\,\mathrm{m\,s^{-1}}$. The recovery phase subsequently occurred over a 15 min duration, ending at 07:40 UTC (14:40 LT), when *hp*F2 returned to the baseline level.

3.2 GPS TEC observations

Figure 8 shows a map depicting the location of four discrete checkpoints where we examined the TEC time series data. These checkpoints are code-named KTB (co-located with the Kototabang station), GEC (point of greatest eclipse), GDU (point of the longest annularity duration), and PTK (co-located with the Pontianak station). By examining the TEC time series at these four fixed checkpoints, we remove some of the ambiguity that may arise from the movement of the IPPs. The TEC values from individual IPPs are spatially interpolated onto the checkpoints using a form of the inverse-distance-weighting (IDW) interpolation technique (Pradipta et al., 2014). The westernmost and easternmost checkpoints (KTB and PTK) were chosen since there are ionosondes at these locations. The other checkpoints (GEC and GDU) were chosen because of the special conditions of the solar-eclipse parameters there. At each checkpoint, time series of absolute TEC and ΔTEC were examined. The ΔTEC values were obtained by subtracting a smooth baseline from the absolute TEC values, which would reveal net changes in TEC relative to normal conditions. The baseline TEC was determined by averaging the TEC values on 25 and 27 December 2019, which are the days prior to and after the solar eclipse. We also determined the upper and lower bounds for the baseline TEC based on the standard deviation of the International Reference Ionosphere (IRI) model output for 18–25 December 2019.

Figure 9 shows the TEC time series plots for 25–27 December 2019 at each of the four designated checkpoints. In these time series plots, the observed TEC values (red curves) are compared to the normal baseline (cyan curves) that rep-

resent the diurnal TEC variation in the absence of a solar eclipse. Over all of these four checkpoints, the TEC responded to the solar eclipse in a relatively similar fashion, with a significant reduction during the eclipse. This TEC reduction was subsequently followed by a recovery that went past the end of the eclipse. In general, the rate of TEC reduction was different for different checkpoints. More notably, although the TEC reduction at all of these four checkpoints happened monotonically, the TEC recovery process was not as monotonic. At certain checkpoints (KTB and GDU), the TEC recovery was quite uneven and occurred in graduated steps. Further, the minimum TEC at each checkpoint was reached with a different time delay relative to the moment of maximum eclipse. The details of these features can be seen more clearly in the ΔTEC time series.

Figure 10 shows the ΔTEC time series plots for 25–27 December 2019 at each of the four designated checkpoints. In comparison to the TEC variation on non-eclipse days, the reduction in TEC during the solar eclipse at these four locations was quite large. The depth of the TEC reduction valley was generally different for each checkpoint. Over checkpoint KTB, the depth of the TEC reduction valley was −4.2 TECU. Over checkpoint GEC, the depth of the TEC reduction valley was −4.5 TECU. Meanwhile, the depth of the TEC reduction valley over checkpoints GDU and PTK was −5.0 and −5.5 TECU, respectively. Among the four designated checkpoints, the smallest reduction was found over KTB. In general, the TEC reduction valley appears to be deeper for checkpoints located further east. In addition, we can also discern the non-monotonicity of the TEC recovery process over these four designated checkpoints, which was exhibited with varying degrees.

A full summary of the observed reduction in TEC over the four designated checkpoints as a response to the eclipse, with some comparison to the corresponding reduction in *fo*F2 (for the KTB and PTK checkpoints), is presented in Table 1. The tabulated information includes the amount of reduction, the time delay between the maximum eclipse and the lowest point in the reduction valley, and the average reduction and recovery rates.

In order to gain a better understanding of the ionospheric response to the solar eclipse beyond the examination of TEC and ΔTEC time series over fixed checkpoints, we also conducted a more elaborate analysis using a set of cross-sectional cut lines. The TEC, ΔTEC, and TECP data along these cross-sectional cut lines are assembled into keograms, which enable us to reveal a greater complexity in the pattern of the ionospheric response to the solar eclipse. The results from this analysis are presented below.

Figure 11 shows a geographical map depicting a set of cross-sectional cut lines that were used for the analysis. One is oriented along the eclipse trajectory, which we refer to as the *parallel evaluation arc*. Meanwhile, the other four are oriented perpendicularly to the eclipse trajectory, which we refer to as *x-cut line* nos. 1–4. These cross-sectional cut lines were chosen according to their proximity to the eclipse trajectory and the availability of GNSS receiver stations. Further, x-cut lines nos. 2 and 4 were chosen to include the coordinates of the Kototabang and Pontianak ionosondes.

Figure 12 shows the keograms for TEC, ΔTEC, and TECP as a function of UTC and longitude along the parallel evaluation arc. The TEC, ΔTEC, and TECP values are indicated using color maps. Figure 12a depicts 2 d (2 × 24 h) worth of data on 25 and 26 December 2019, whereas Fig. 12b shows a magnification around the period of the solar eclipse. In Fig. 12a.i, the normal diurnal pattern of TEC variation at various longitudes in the absence of a solar eclipse can be recognized from the first half of the data (covering 25 December 2019). During the solar eclipse (the period marked by the dashed/dotted lines on 26 December 2019), the pattern of TEC reduction was highly visible since, at this time of the day, TEC would normally have neared its daily maximum level. Figure 12b.i offers a greater visual detail. The pattern of eclipse-related TEC reduction along the parallel evaluation arc was generally found to be uneven. In the longitude span from 90 to 102° E during the eclipse, TEC was considerably lower than that at other longitudes. This uneven pattern in TEC reduction is likely due to the difference in solar local time at various points along the parallel evaluation arc when the solar eclipse happened.

In Fig. 12a.ii, we show the ΔTEC as a function of UTC and longitude along the parallel evaluation arc. Similar to the case of the four fixed checkpoints, the ΔTEC values were obtained by subtracting a smooth baseline from the absolute TEC values. However, in this case the smooth baseline for each individual longitude was determined by taking the average of the corresponding TEC data from the entire month (excluding 18–20 and 26 December 2019 due to geomagnetic activity and the solar eclipse). During the initial phase of the eclipse, the decrease in ΔTEC did not immediately take place. The drop in ΔTEC below zero only started when the time was approaching the maximum eclipse. At its lowest, ΔTEC reached approximately −6 TECU. The negative ΔTEC remained until the end of the eclipse. Figure 12b.ii offers a greater visual detail. We also recognized that the pattern of reduction in ΔTEC was highly uneven. The duration of the ΔTEC reduction valley varied slightly across different longitudes. However, more notably, over the longitude span from 96 to 107° E, the ΔTEC reduction valley was visibly not as deep as in other locations. This "shallow ΔTEC valley" occurred over Sumatra, which is a major land mass traversed by the solar eclipse. The precise cause of this shallow valley is uncertain at this point.

In Fig. 12a.iii, we show the TECP as a function of UTC and longitude along the parallel evaluation arc. The TECP was derived through a detrending process. However, unlike ΔTEC previously, here the TEC data detrending was performed on the IPPs before we spatially interpolated the detrended values onto the cross-sectional cut lines. The TECP values on individual IPPs were obtained by subtracting the

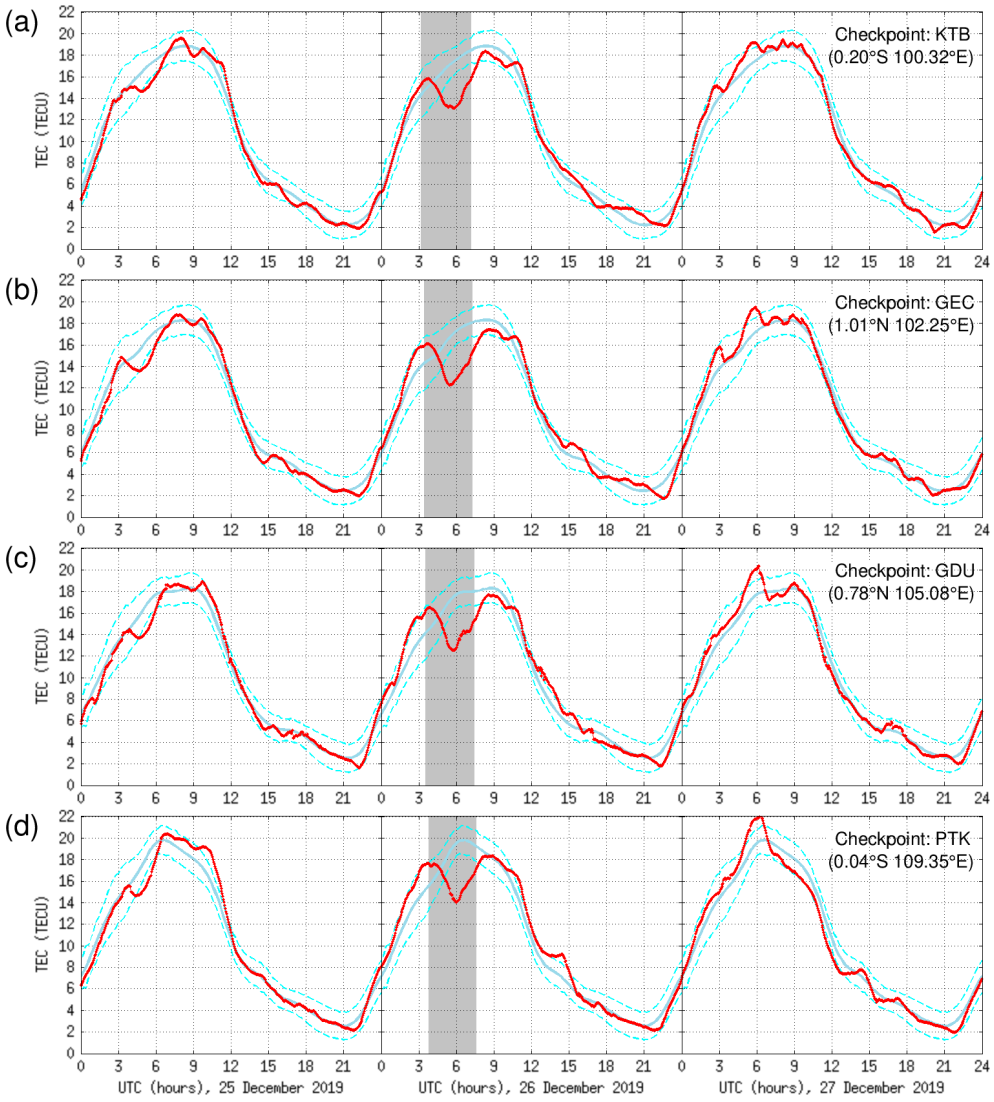

Figure 9. (a–d) Time series plots of GPS TEC at the four designated checkpoints (KTB, GEC, GDU, and PTK) on 25–27 December 2019. Smooth background TEC levels based on the 25 and 27 December 2019 data, combined with IRI model runs on 18–25 December 2019, are shown in cyan. Observation data are shown in red. The solar eclipse period is indicated with gray bands.

30 min running average. After detrending, the TECP values were spatially interpolated onto the parallel evaluation arc using the IDW technique. Generally speaking, there are wavelike fluctuations in the TECP data at nearly all times of the day. However, there were recognizable changes in the TECP pattern that matched the period of the solar eclipse. These distinct wavelike fluctuation patterns persisted until the end of the eclipse. The characteristics of the wavelike fluctuation patterns varied during different phases of the solar eclipse. From the start of the eclipse until the maximum eclipse, there was a wavelike fluctuation pattern where the average TECP was biased toward positive polarity. At the maximum eclipse, the TECP values dipped sharply to become negative. Finally, from the maximum eclipse until the end of the eclipse, there was another wavelike fluctuation pattern, but this time with the average TECP slightly biased toward negative polarity.

Figure 13 shows keograms of TEC values as a function of UTC and latitude along the four x-cut lines, covering the time interval 01:00–09:00 UTC on 25–27 December 2019 in different rows. A reduction in the TEC values can be seen along each of the four x-cut lines during the solar eclipse. At each x-cut line, however, there was a different time delay from the start of the eclipse (C1) until a significant decrease in TEC started to happen. This time delay ranged between 1 and 2 h. The TEC reduction occurred predominantly to the north of the greatest eclipse point for each x-cut line.

Figure 14 shows keograms of ΔTEC values as a function of UTC and latitude along the four x-cut lines, covering the time interval 01:00–09:00 UTC on 25–27 December 2019 in

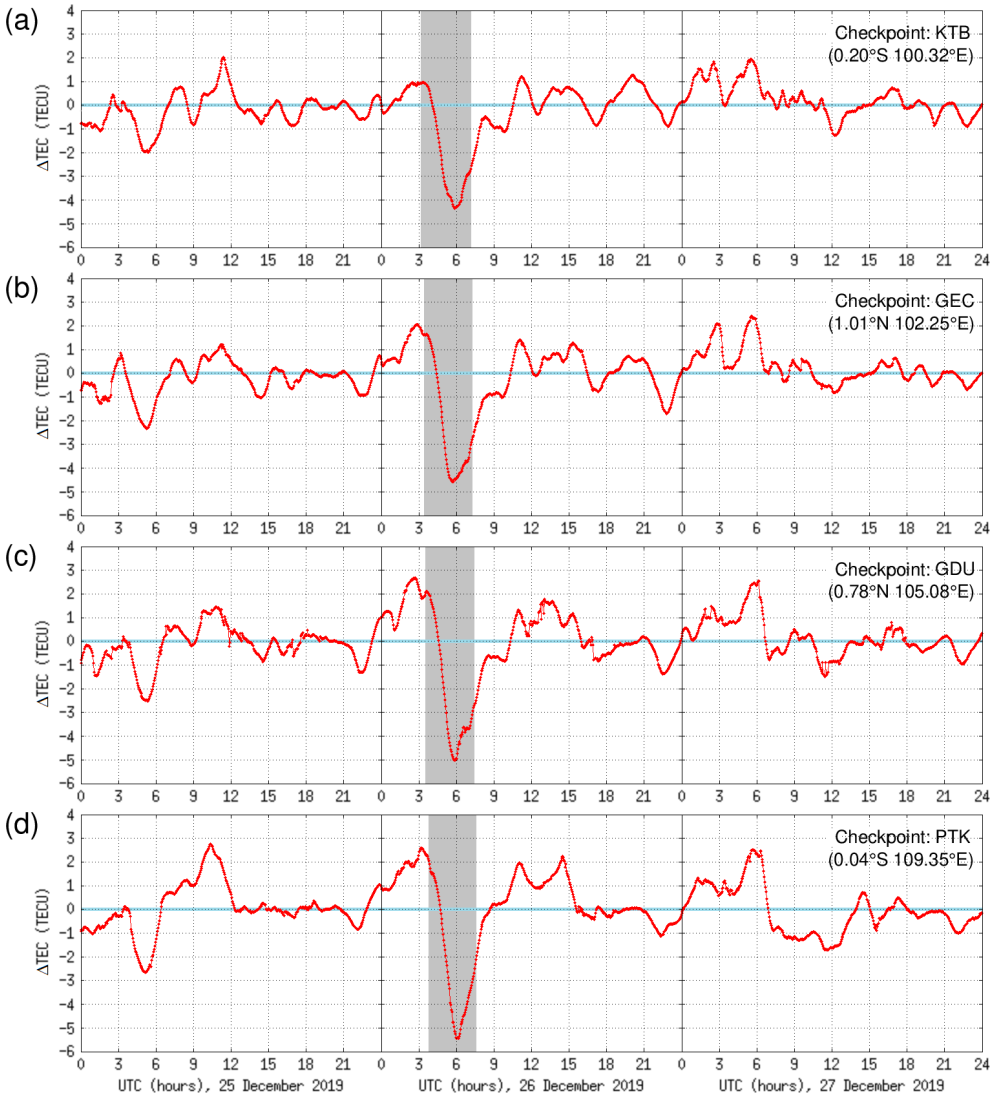

Figure 10. (a–d) Time series plots of ΔTEC at the four designated checkpoints (KTB, GEC, GDU, and PTK) on 25–27 December 2019, obtained by subtracting the smooth background TEC level from the GPS TEC observation data. The solar eclipse period is indicated with gray bands.

different rows. The patterns of TEC reduction along each of the four x-cut lines during the eclipse are more clearly visible in this case. These keograms confirm that the TEC reduction occurred more predominantly to the north of the greatest eclipse point for each x-cut line. This is signified by the ΔTEC in the northern part of the x-cut lines being more negative than that in the southern part.

Figure 15 shows keograms of TECP values as a function of UTC and latitude along the four x-cut lines, covering the time interval 03:00–08:00 UTC on 25–27 December 2019 in different rows. At the time of maximum eclipse, the TECP values in the keogram formed a prominent trough that is oriented parallel to the maximum eclipse line. Meanwhile, along x-cut no. 3, a convex bulge with a positive TECP polarity was seen between latitudes −5 and 0° just after the C1 phase. The convex bulge lasted for approximately 30 min. The tip of this bulge started at latitude −2°, and the rest of this bulge then widened north to south, resembling a left-facing wavefront. Between C1 and C4, there were a number of striped patterns that indicate oscillations in the TECP data. The contours of these striped patterns were oriented roughly parallel to the contours of the C1 and C4 epoch lines. These wavelike fluctuations might be caused either by intrinsic nonuniformity (wrinkles) embedded in the solar EUV irradiance patterns or by traveling ionospheric disturbances (TIDs) generated during the eclipse. The closer the alignment of the stripe patterns to the C1/max/C4 epoch lines, the more likely they are to be associated with the EUV modulation mechanism. The further away the striped patterns

Table 1. Summary of observed changes in *fo*F2 and TEC at the four designated checkpoints (cf. Fig. 8) due to the passage of annular solar eclipse over Indonesia on 26 December 2019.

Site information	*fo*F2 reduction	Minimum *fo*F2	*fo*F2 recovery	TEC reduction and recovery
KTB eclipse timing: start 03:18 UTC, max 05:11 UTC, (obsc = 91.0 %), end 07:08 UTC.	04:35–05:45 UTC (duration: 70 min) Initial *fo*F2 = 6.70 MHz (5.5×10^5 el cm^{-3}) *fo*F2 reduction rate = −1.03 MHz h^{-1} (−43 el cm^{-3} s^{-1})	Min *fo*F2 = 5.50 MHz reached at 05:45 UTC Δ*fo*F2 = −1.62 MHz[a] (24.0 % relative reduction[a]) Time lag = 34 min[b]	05:45–08:45 UTC (duration: 180 min) Final *fo*F2 = 7.10 MHz (6.2×10^5 el cm^{-3}) *fo*F2 recovery rate = +0.53 MHz h^{-1} (+23.0 el cm^{-3} s^{-1})	Min ΔTEC = −4.34 TECU[a] reached at 05:51 UTC (24.9 % relative reduction[a]) Time lag = 40 min[b] Reduction rate = −4.06 TECU h^{-1} Recovery rate = +3.13 TECU h^{-1}
GEC eclipse timing: start 03:23 UTC, max 05:18 UTC (obsc = 94.1 %), end 07:14 UTC.	NA	NA	NA	Min ΔTEC = −4.58 TECU[a] reached at 05:42 UTC (27.0 % relative reduction[a]) Time lag = 24 min[b] Reduction rate = −5.63 TECU h^{-1} Recovery rate = +2.81 TECU h^{-1}
GDU eclipse timing: start 03:31 UTC, max 05:28 UTC (obsc = 94.1 %), end 07:22 UTC.	NA	NA	NA	Min ΔTEC = −5.01 TECU[a] reached at 05:51 UTC (28.5 % relative reduction[a]) Time lag = 23 min[b] Reduction rate = −5.91 TECU h^{-1} Recovery rate = +3.99 TECU h^{-1}
PTK eclipse timing: start 03:45 UTC, max 05:44 UTC (obsc = 93.0 %), end 07:32 UTC.	04:50–06:20 UTC (duration: 90 min) Initial *fo*F2 = 6.21 MHz (4.6×10^5 el cm^{-3}) *fo*F2 reduction rate = −0.51 MHz h^{-1} (−20.6 el cm^{-3} s^{-1})	Min *fo*F2 = 5.44 MHz reached at 06:20 UTC Δ*fo*F2 = −1.90 MHz[a] (27.5 % relative reduction[a]) Time lag = 36 min[b]	06:20–08:55 UTC (duration: 155 min) Final *fo*F2 = 6.67 MHz (5.5×10^5 el cm^{-3}) *fo*F2 recovery rate = +0.48 MHz h^{-1} (+19.9 el cm^{-3} s^{-1})	Min ΔTEC = −5.45 TECU[a] reached at 06:00 UTC (27.9 % relative reduction[a]) Time lag = 16 min[b] Reduction rate = −5.64 TECU h^{-1} Recovery rate = +4.54 TECU h^{-1}

[a] Change in ionospheric quantity measured relative to the baseline curve (rather than to the pre-eclipse initial value). [b] Time delay since the point of maximum eclipse until the said ionospheric quantity reached minimum. NA – not available.

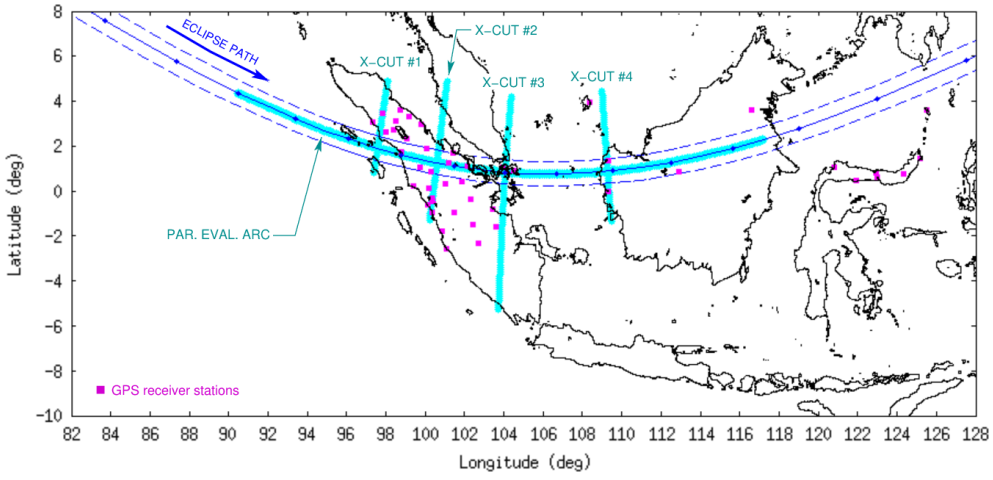

Figure 11. Geographical map showing a set of cut lines, along and perpendicular to the solar-eclipse path, for an extended analysis of TEC variation in response to the eclipse. The cut line along the eclipse path is referred to as the *parallel evaluation arc*, and those perpendicular to the eclipse path are referred to as *x-cut* nos. 1 to 4.

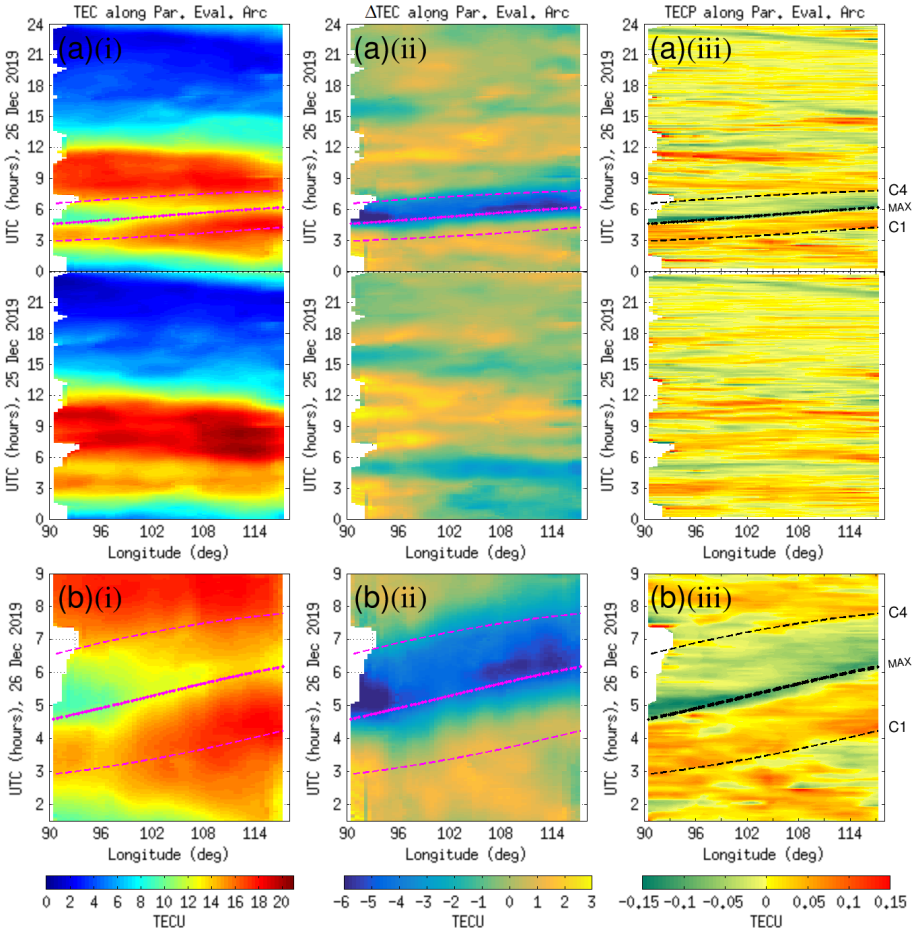

Figure 12. Color-map plots of GPS TEC, ΔTEC, and TECP values as a function of time and longitude along the parallel evaluation arc **(a)** within a 48 h time interval on 25 and 26 December 2019 and **(b)** within a magnified time interval around the solar eclipse on 26 December 2019. The start and end times of the eclipse (C1 and C4) as well as the moment of maximum eclipse are indicated by dashed and dotted curves on the plots.

were from the alignment with the C1/max/C4 epoch lines, the more likely they are to be associated with a TID.

3.3 Solar EUV illumination variability

During the 26 December 2019 annular solar eclipse over the Indonesian sector, the Moon's umbra moved from west to east with a ground speed of approximately 1.1 km s^{-1} (Espenak, NASA GSFC, 2019). Despite this high speed, temporal and spatial variation in the solar EUV irradiance over eclipse-affected areas still happened gradually in stages. With a finite width of the eclipse central path (i.e., the umbra) of approximately 117–120 km, partial and annular eclipse also occurred consecutively along the eclipse central path in a gradual manner. Using the Laplacian as the main metric, we are able to capture the inhomogeneity in the solar EUV irradiance. This characterization was performed by computing the Laplacian of the solar EUV irradiance at various point locations at each epoch, which enabled us to map its full spatiotemporal evolution.

Figure 16 shows the pattern of the Laplacian of solar EUV irradiance calculated over a region that spans from longitude 70 to 150° E and from latitude 30° S to 30° N, evaluated at different times during the passage of the solar eclipse. From these snapshots, we can see the spatial variation of solar EUV irradiance that was present during the eclipse, which generally resembles the outline of the lunar shadow as it traversed across the region. Moreover, there were also signatures of ARs on the Sun's surface in the spatial inhomogeneity of solar EUV irradiance received on Earth. They appear as smaller ring patterns within the greater outline of the lunar shadow in the EUV Laplacian map. All of these patterns moved across the region, with velocity matching that of the lunar shadow.

Figure 17 shows the calculated spatiotemporal pattern of the EUV Laplacian along the parallel evaluation arc. From this contour/color-map plot, we can see how the solar EUV irradiance variation was spatiotemporally consistent with the

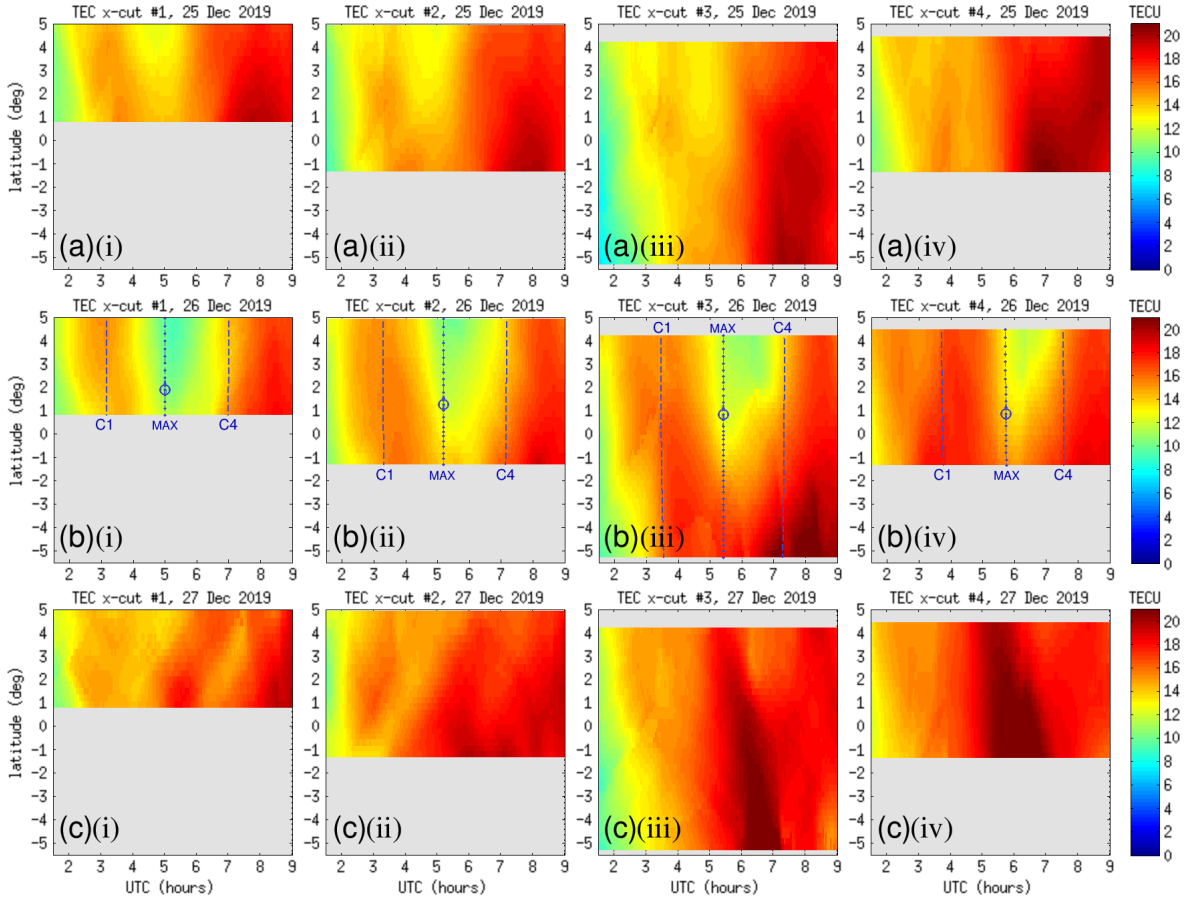

Figure 13. Color-map plots of GPS TEC values as a function of time and latitude along x-cut nos. 1 to 4 on **(a)** 25, **(b)** 26, and **(c)** 27 December 2019. Time intervals are magnified around the solar eclipse on 26 December 2019. The start and end times of the eclipse (C1 and C4) as well as the moment of maximum eclipse are indicated by dashed and dotted curves on the plots. Circles indicate the moment and location of the greatest solar obscuration along each x-cut.

timing of various eclipse phases. Outside of the eclipse period, there was no fluctuation in the Laplacian because all the ARs would have been fully visible from every point on Earth that was facing the Sun.

Figure 18 shows contour/color-map plots of the Laplacian of the solar EUV irradiance variation along x-cut line nos. 1 to 4 as a function of time and latitude, which exhibit some of the same basic patterns. As in the case of the parallel evaluation arc, there was no fluctuation in the Laplacian outside of the eclipse period. One major difference here is that there was a set of distinct features around the greatest eclipse point for each x-cut line, which appear as pairs of pod-shaped blobs that sandwiched the annularity region. In Fig. 18c and d, they resembled a macaron around the annularity region.

Although the basic outlines of the Laplacian of solar EUV irradiance found in Figs. 17 and 18 are generally consistent with the TECP profiles shown in Figs. 12 and 15, there are some important differences in the details of the patterns. We found that some of the large structures observed in the TECP profile were not part of the EUV Laplacian profile. Furthermore, several fine structures that appeared in the EUV Laplacian profile did not actually materialize in the TECP profile. More detailed discussion regarding the relations between the TECP and EUV Laplacian profiles is presented in Sect. 4.

4 Discussion

Throughout December 2019, the most-disturbed geomagnetic condition occurred on 18–20 December 2019, with the lowest Dst index of -28 nT (World Data Center at Kyoto University) and the highest Kp index of 4^- (GFZ Potsdam). During the solar-eclipse day (26 December 2019), the geomagnetic condition was quiet, with the lowest Dst index of -6 nT and the highest Kp index of 2^+. Thus, in general, the effect of geomagnetic activity may be neglected in the analysis of the solar-eclipse effects on the ionosphere. The F10.7 solar-flux index on the eclipse day was approximately 70 sfu (NASA OMNIWeb Database), and this value was quite stable during ± 3 d prior to and after the solar-eclipse day. There

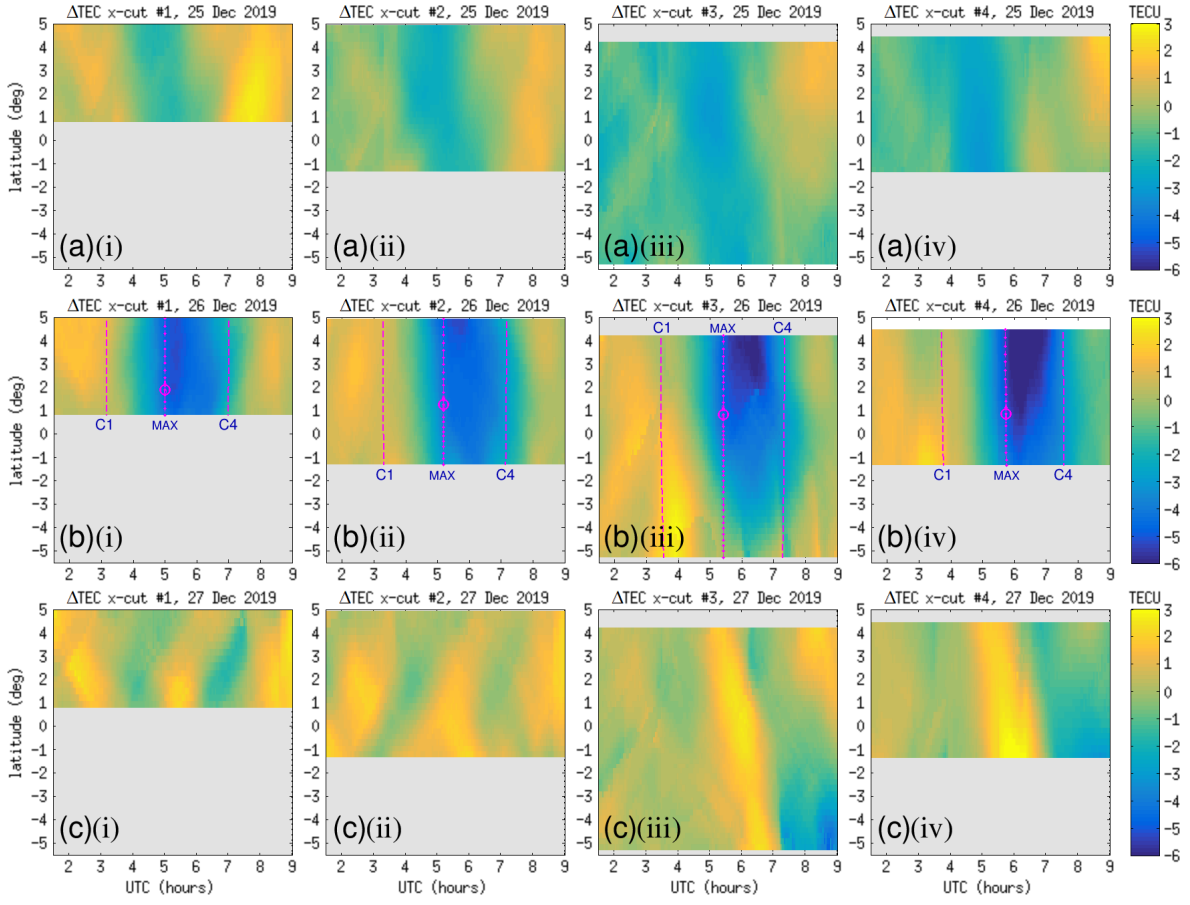

Figure 14. Color-map plots of ΔTEC values as a function of time and latitude along x-cut nos. 1 to 4 on **(a)** 25, **(b)** 26, and **(c)** 27 December 2019. Time intervals are magnified around the solar eclipse on 26 December 2019. The start and end times of the eclipse (C1 and C4) as well as the moment of maximum eclipse are indicated by dashed and dotted curves on the plots. Circles indicate the moment and location of the greatest solar obscuration along each x-cut.

were no major changes in the background solar flux that may significantly confound the solar-eclipse effect.

The ionospheric time delay between the moment of maximum eclipse and minimum *fo*F2 over KTB was 34 min, and that over PTK was 36 min. This time delay is shorter than the time delay from a number of other studies: Jose et al. (2020) reported a time delay of 1 h, Adeniyi et al. (2007) reported a time delay of 40 min, Dear et al. (2020) reported a time delay of 1 h, and Bravo et al. (2020) reported time delays of 4, 40, and 62 min. The shorter time delay may be caused by the longer eclipse duration as a whole. The overall eclipse duration over KTB was 4 h, and that over PTK was 3 h 47 min. Meanwhile, the duration of solar-eclipse events studied by Adeyini et al. (2007) and Dear et al. (2020) was about 2 h. This difference in the overall eclipse duration may be the reason behind the significant difference in the time delay.

The average rates of *Nm*F2 (*fo*F2) reduction over KTB and PTK were 43.0 el cm^{-3} s^{-1} (1.03 MHz h^{-1}) and 20.64 el cm^{-3} s^{-1} (0.51 MHz h^{-1}), respectively. The relative *fo*F2 reductions with respect to the baseline level were 24.0 % over KTB (where the maximum obscuration was 91 %) and 27.5 % over PTK (where the maximum obscuration was 93 %). This relative reduction is slightly smaller in magnitude than the eclipse-induced reduction reported in the past by Adeniyi et al. (2007) of 54 % and that by Dear et al. (2020) of 30 %–40 %. This difference may have been influenced by the type of solar eclipse that occurred and the actual local time of the solar-eclipse event. The 26 December 2019 annular solar eclipse occurred later in the day (10:20–14:30 LT) when compared to the eclipse event investigated by Adeniyi et al. (2007), which occurred between 09:00 and 11:00 LT, and that investigated by Dear et al. (2020), which occurred between 08:46 and 11:40 LT. The local time of the eclipse event mattered, since, the closer we are to noontime, the stronger the equatorial fountain effect tends to be. This proclivity is also mimicked by the strength of the equatorial electrojet (EEJ) at noon, which is stronger than the pre-noon EEJ. As such, a stronger plasma flow associated with the equatorial fountain effect at midday might affect the amount of eclipse-induced *fo*F2 reduction by its influence on

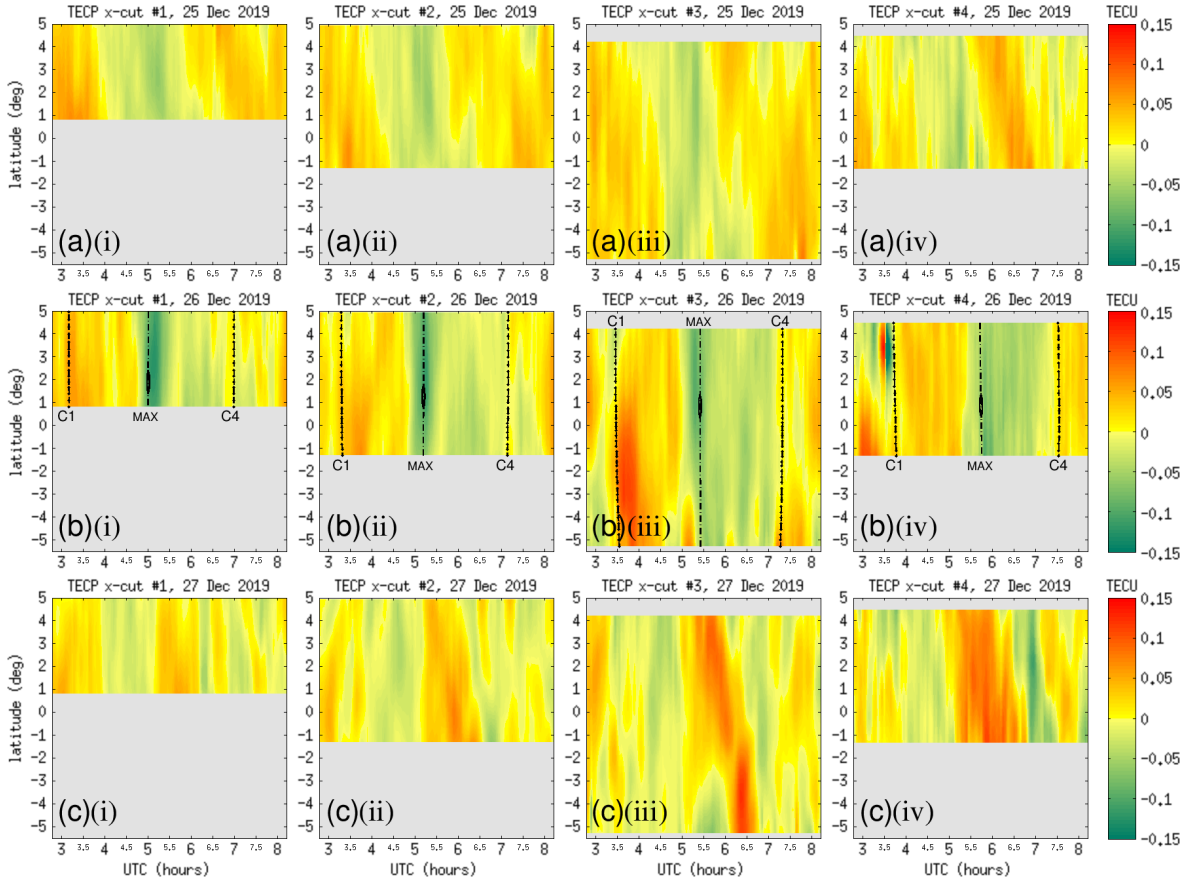

Figure 15. Color-map plots of TECP values as a function of time and latitude along x-cut nos. 1 to 4 on **(a)** 25, **(b)** 26, and **(c)** 27 December 2019. Time intervals are magnified around the solar eclipse on 26 December 2019. The start and end times of the eclipse (C1 and C4) as well as the moment of maximum eclipse are indicated by dashed curves on the plots. The small bulge on the maximum eclipse line indicates the annularity region.

the transport process. The 26 December 2019 annular solar eclipse occurred around noontime, during which the equatorial fountain may have lessened the amount of *fo*F2 reduction to some degree since both KTB and PTK are located near the southern crest of the equatorial ionization anomaly (EIA).

The average recovery rates of the *Nm*F2 value over KTB and PTK were 23.04 and 19.9 el cm^{-3} s^{-1}, which occurred during the time intervals 05:45–08:45 and 06:20–08:55 UTC, respectively. The respective time delay between the end of the eclipse and the end of the recovery phase over KTB and PTK were 97 and 83 min. The relatively long time delay until the completion of the recovery phase might be caused by the additional influence of the transport and diffusion processes that slowed down the rate of plasma accumulation from direct photoionization.

The observed *fo*F2 (and *Nm*F2) reduction and recovery over PTK in general exhibited a symmetrical pattern. Meanwhile, over KTB, the pattern was not so symmetrical: the rate of *fo*F2 reduction was steeper than the rate of *fo*F2 recovery. Based on the findings reported in past studies (e.g., Farges et al., 2001; Adeniyi et al., 2007; Goncharenko et al., 2018), a symmetrical *fo*F2 reduction/recovery pattern is more common. Hence, the pattern observed over KTB during this solar-eclipse event was somewhat abnormal. Considering that the *fo*F2 recovery rate over KTB was quite similar to that over PTK, the abnormality over KTB can be attributed to the *fo*F2 reduction rate. In other words, the *fo*F2 reduction rate over KTB was steeper than normally expected. The reason for a steeper *fo*F2 reduction rate over KTB was most likely the higher initial *fo*F2 (and *Nm*F2) value at the start of the eclipse, which resulted in a higher recombination rate in the absence of photoionization viz. $\mathrm{d}N/\mathrm{d}t = -\alpha N^2$ in the ionization balance equation (Rishbeth, 1963, 1968; Rishbeth and Garriott, 1969; Adeniyi et al., 2009).

The level of reduction in *fo*F2 (and *Nm*F2) during an eclipse is expected to be proportional to the level of obscuration. For a greater obscuration, the recombination process would overcome the photoionization process (Adeniyi et al., 2009). On the other hand, for low obscuration (e.g., in places far from the main eclipse path), the level of reduction in *fo*F2 due to the eclipse would not be as prominent. Resende et al. (2022) analyzed observation data from

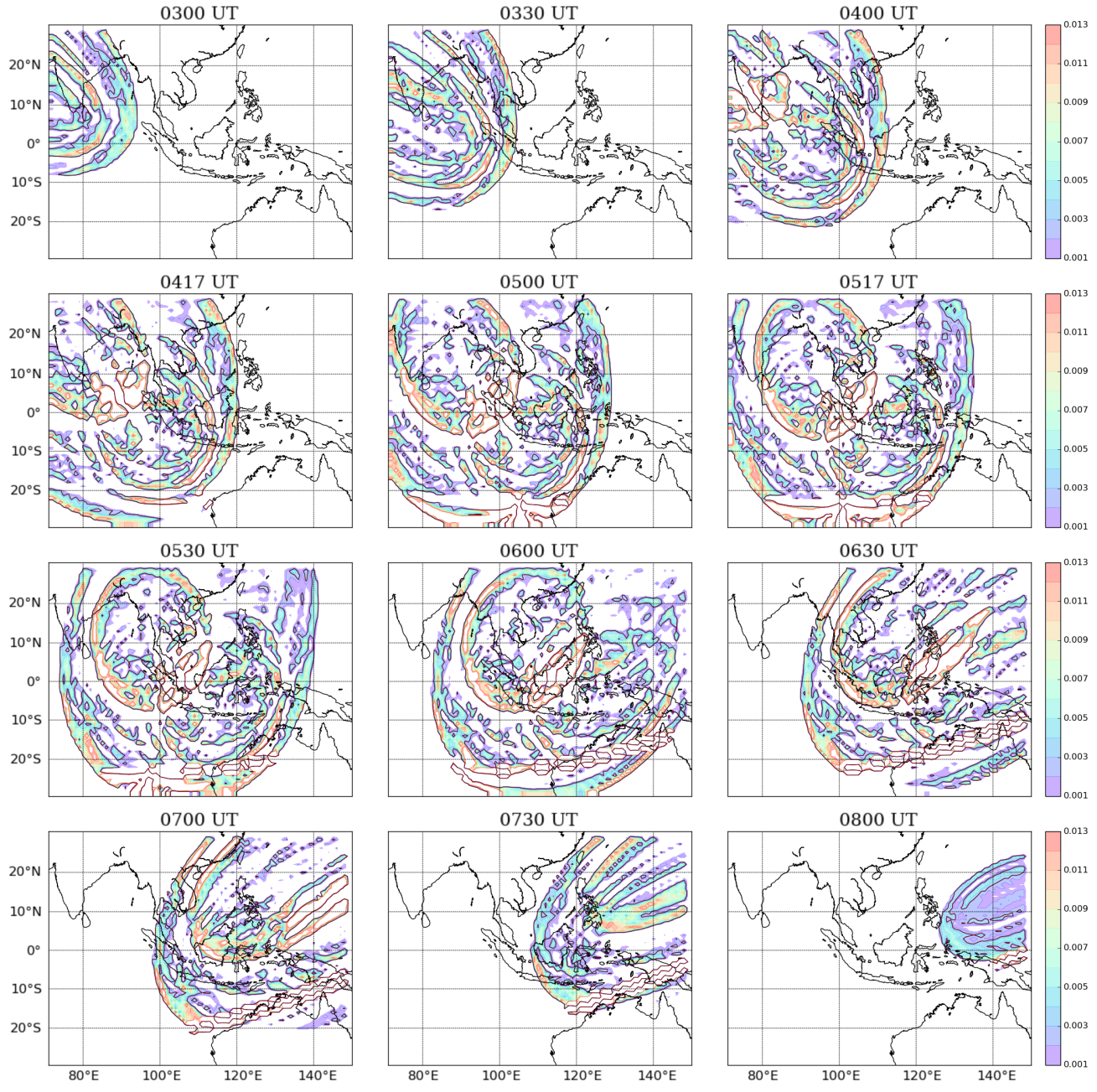

Figure 16. Sequential snapshots of spatial inhomogeneities in the solar EUV illumination pattern over Southeast Asia on 26 December 2019 as the annular solar eclipse traversed through the region. Contours and color map indicate the absolute magnitude of the Laplacian of the solar EUV irradiance distribution over a geographic latitude–longitude grid at 100 km altitude.

the Campo Grande (CG; 20.47° S, 54.60° W; dip latitude ∼ 23° S) and Cachoeira Paulista (CXP; 22.70° S, 45.01° W; dip latitude ∼ 35° S) stations, located in a low-latitude region in Brazil, during the 14 December 2020 solar eclipse. The two stations are quite far from the main eclipse path, and the obscuration level is only around 20 %–30 %. They found a reduction in the foE value and a disappearance of the F1 region during the eclipse but did not find a significant reduction in the *fo*F2 value.

In terms of changes in *fo*F1 during the eclipse, the time delay between maximum eclipse and minimum *fo*F1 over KTB and PTK was 9 and 16 min, respectively. This relatively short response time confirms that the ionospheric F1 layer is dominated by a production/loss mechanism involving a direct photoionization and recombination process, and it is not affected significantly by transport processes (Farges et al., 2001; Jose et al., 2020).

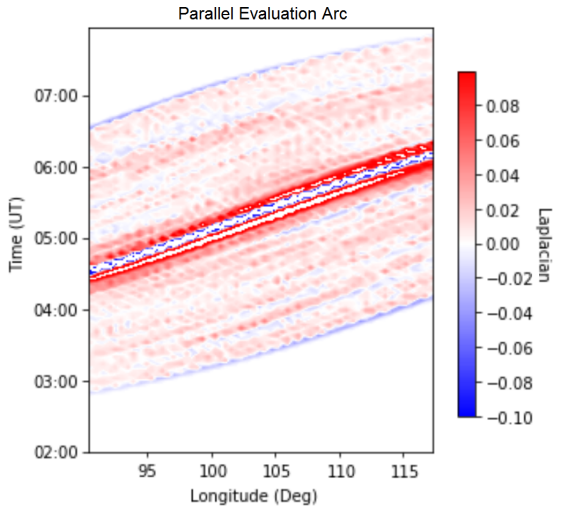

Figure 17. Contour/color-map plot of the Laplacian of the solar EUV irradiance level at 100 km altitude as a function of time and longitude along the parallel evaluation arc, within a magnified time interval around the solar eclipse on 26 December 2019.

The relative *fo*F1 reduction with respect to the baseline level was 33 % over KTB and 27 % over PTK. This relative *fo*F1 reduction is similar to that reported by Jose et al. (2020), which showed a relative *fo*F1 reduction of 29 % over Trivandrum, India (8.5° N, 77° E; 0.5° N magnetic latitude (MLAT), during the 15 January 2010 annular solar eclipse when the solar cycle was heading away from a minimum towards a maximum. In contrast, Adeniyi et al. (2007) showed a relative *fo*F1 reduction of 68 % over Ilorin, Nigeria (8.53° N, 4.57° E; 4.1° S MLAT), during the 29 March 2006 total solar eclipse during a minimum phase of the solar cycle. The significant difference in the findings of Adeniyi et al. (2007) might be due to the different type of solar eclipse that occurred. The average rate of *fo*F1 reduction over KTB was $-16\,\mathrm{el\,cm^{-3}\,s^{-1}}$, and that over PTK was $-29\,\mathrm{el\,cm^{-3}\,s^{-1}}$. The much steeper *fo*F1 reduction rate over PTK was most likely due to a higher initial *fo*F1 value, which resulted in a higher recombination rate ($\mathrm{d}N/\mathrm{d}t = -\alpha N^2$) in the absence of photoionization (Cheng et al., 1992; Adeniyi et al., 2009).

The average rates of *fo*F1 recovery over KTB and PTK were 44.0 and 15.49 $\mathrm{el\,cm^{-3}\,s^{-1}}$, which occurred during the time intervals 05:20–06:25 UTC and 06:00–07:20 UTC, respectively. The difference between the rates of *fo*F1 recovery over these two locations may look striking, with nearly a 3 : 1 ratio. However, considering the spread of data points (2.90–3.53 MHz) near the minimum *fo*F1 value over KTB stations, the registered recovery rate of 44.0 $\mathrm{el\,cm^{-3}\,s^{-1}}$ is actually associated with a fairly large range of uncertainty (plausible range of recovery rate: 31–44 $\mathrm{el\,cm^{-3}\,s^{-1}}$). Thus, the difference in the average *fo*F1 recovery rate between KTB and PTK may in fact be milder, with a ratio closer to 2 : 1, similar to the difference in the *fo*F1 reduction rate between PTK and KTB.

The *fo*F2 time series on 26 December 2019 showed an overshoot during the recovery phase beyond the baseline level in the time interval 08:45–10:30 UTC (15:45–17:30 LT) over KTB and in the time interval 09:05–10:30 UTC (16:05–17:30 LT) over PTK. The *fo*F2 overshoot had a magnitude of 0.5–0.7 MHz above the baseline level. This overshoot might have been caused by an inward shift of the EIA crest position during the post-eclipse period after an outward shift that happened earlier during the eclipse (Aa et al., 2020). This outward shift was explained in terms of an enhanced eastward polarization electric field during the eclipse, which strengthened the equatorial fountain and made the fountain flow land over greater |MLAT| locations (Aa et al., 2020). The present TEC data (cf. Fig. 13b.iii) confirmed this momentary outward shift of the EIA crest during the eclipse. The TEC data also indicate that the EIA crest returned to a normal configuration a few hours after the eclipse ended. This is consistent with the fountain returning to normal strength as the enhanced polarization electric field diminished. The shift in the EIA crest back to its original position (and fountain flow returning to normal) happened simultaneously with the local recovery of *fo*F2 by the restored photoionization, causing *fo*F2 to overshoot its baseline value. A similar but less prominent feature was also observed in terms of the *fo*F1 parameter, possibly for the same reason. Further, we note that an overshoot feature in *fo*F2 values was also observed during the 21 August 2017 solar eclipse over a mid-latitude region (Goncharenko et al., 2018).

Examination of *fo*F1 time series on 26 December 2019 over PTK revealed a momentary increase in the *fo*F1 value before it eventually decreased in response to the solar eclipse. The magnitude of the aforementioned increase was only ~ 0.25 MHz, with a duration of ~ 30 min. This particular feature is similar to past findings reported by Anastassiades and Moraitis (1968) and Jonah et al. (2020). This peculiar feature is thought to be caused by diffusion of electrons from the topside altitudes above hmF1 as the electron temperature remains greater than the neutral temperature during a solar eclipse. It is believed that this feature can only occur for a solar-eclipse event that happens in the minimum phase of the solar cycle. The said feature was not found in the *fo*F1 time series data over KTB.

In terms of general timing, we note here that the eclipse-related *fo*F1 reduction and recovery occurred completely within the eclipse phase, whereas the eclipse-related *fo*F2 reduction and recovery extended well beyond the eclipse period. This pattern reaffirms the established concept that there are different plasma production and loss mechanisms operating in the ionospheric F1 and F2 layers (Rishbeth and Garriott, 1964, 1969; Rishbeth, 1968; Hargreaves, 1992). Plasma density in the ionospheric F1 layer is largely determined by photoionization and recombination only. Meanwhile, plasma density in the ionospheric F2 layer is influenced not only by

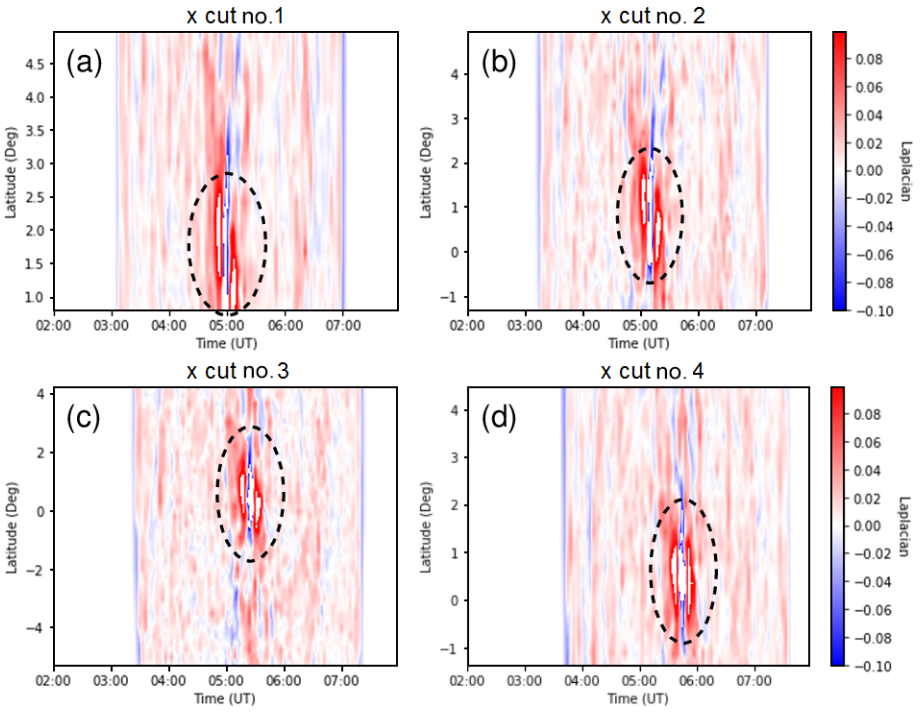

Figure 18. (a–d) Contour/color-map plot of the Laplacian of the solar EUV irradiance level at 100 km altitude as a function of time and latitude along x-cut nos. 1 to 4, within a magnified time interval around the solar eclipse on 26 December 2019. Dashed circles highlight the characteristic pairs of pod-shaped blob patterns that appear in the vicinity of the annularity region.

photoionization and recombination, but also by the transport process.

Over KTB, *hp*F2 was observed to decrease roughly 2 min after the start of the eclipse. Meanwhile, over PTK, *hp*F2 started to decrease roughly 10 min after the start of the eclipse. The "downward motion" of *hp*F2 occurred for approximately 95 min over KTB (a 50 km overall descent) and 120 min over PTK (a 136 km overall descent). The observed decrease in *hp*F2 is probably only a "downward spatial relocation" of the altitude where the greatest electron density was found, as the general shape of the electron-density profile changed during the eclipse. Without measurements of the Doppler shift, it is hard to ascertain whether an actual downward plasma motion was present.

Over KTB, *hp*F2 started to rise 19 min after the maximum eclipse, and *hp*F2 reached its highest value of 682 km (220 km higher than the baseline height) at approximately 06:40 UTC (13:40 LT). Later on, *hp*F2 dropped back to the baseline height at approximately 07:00 UTC (14:00 LT) while still within the eclipse period. Meanwhile, over PTK, *hp*F2 started to rise 11 min after the maximum eclipse; and *hp*F2 reached its highest value of 747 km (326 km higher than the baseline height) at approximately 07:35 UTC (14:35 LT). Later on, *hp*F2 value returned to the baseline height at approximately 08:10 UTC (15:10 LT). Possible cause of this increase in *hp*F2 includes: (1) changing shape of electron density profile during the recovery phase that resulted in a "spatial relocation" of the altitude with largest electron density, and (2) an actual upward movement of the ionospheric F2 layer due to a polarization electric field that formed between west and east sides of the eclipse-affected region, which induced a vertical $\boldsymbol{E} \times \boldsymbol{B}$ drift (Jakowski et al., 2008; Le et al., 2009; Adekoya et al., 2015).

With regard to the TEC observation data, there are a few things of note. These include the spatial inhomogeneity in the depths of the TEC reduction valley along the main eclipse trajectory, the spatial inhomogeneity in the depths of the TEC reduction valley in the direction perpendicular to the main eclipse trajectory, and the general relations between the TEC variation during the solar eclipse and the detailed shape of the solar EUV illumination profile.

Based on the observed ΔTEC along the parallel evaluation arc (cf. second column of Fig. 12), we can discern that the ΔTEC values between longitude 96 to 106° E were not as deep as ΔTEC at other locations that were also along the eclipse trajectory, even though they all roughly experienced the same level of solar obscuration and eclipse duration. This feature can only be seen clearly in the ΔTEC data, but not in the absolute TEC data as the absolute TEC contains a mixture of both the diurnal variations and the eclipse response. Definitive reason behind this "shallow ΔTEC valley" is not so clear, but we believe that it involved a physical mechanism, and it was not simply an instrumental effect. A few scenarios involving instrumental artefact can be eliminated.

One such scenario was a systematic shift in the receiver TEC bias for a group of GNSS receiver stations. However, each receiver device operates independently even for closely spaced stations, which makes it highly unlikely for their biases to be electronically linked. The GNSS receiver stations in the region are not uniformly distributed, but spatial distribution of receiver stations are not expected to affect TEC bias calibration. Another scenario under consideration was that the slant factor may be quite extreme (at low elevation angles) for IPPs over the ocean region with no or very few receiver stations, potentially corrupting the slant-to-vertical conversion for a locally depleted ionospheric layer. This scenario predicts that the "shallow TEC valley" would have happened over the ocean region. However, the "shallow TEC valley" was in fact found over land mass (well-populated with receiver stations), contrary to what this scenario predicts. Hence, we can rule out systematic bias shift and extreme slant factor as the root cause of the "shallow TEC valley" feature. As such, a few major instrumental artefacts have been ruled out, and the question regarding the responsible physical mechanism remains open.

In addition to the variation in the depth of ΔTEC valley in east-west direction along the eclipse trajectory, there was also a notable north-south variation in the TEC and ΔTEC valley depths along the four x-cut lines as a function of orthogonal distance from the main eclipse trajectory (cf. Figs. 13 and 14). Somewhat counterintuitively, the lowest TEC and ΔTEC values actually occurred to the north of the eclipse trajectory, even though the lunar shadow was coming from a southerly direction with solar zenith angle of $\sim 23^\circ$ during the eclipse event. Hence this effect cannot be explained simply by the slight obliquity of the lunar shadow relative to vertical direction. Instead, this effect was probably induced by the equatorial fountain effect which transports plasma from magnetic equator area (located north of the eclipse trajectory) to regions at $\pm 15^\circ$ MLAT, effectively providing buffer for the TEC in the area south of the eclipse trajectory. As a result of this siphoning, the area north of the eclipse trajectory was left with a greater deficit in TEC. Such a role of the fountain effect during a solar eclipse over low-latitude region is consistent with findings reported by Aa et al. (2020).

Further, there are some temporal inhomogeneity and fluctuation patterns in the TEC observation data as well. The TEC and ΔTEC data at various observation points indicate that the rate of TEC decrease and increase during the eclipse was generally not symmetrical. Overall, the rate of TEC decrease is greater in magnitude than the rate of TEC increase/recovery. This asymmetric pattern may bear some relations to the shape of the solar EUV illumination profile, which itself also shows some asymmetry. In addition, it is also conceivable that kinks/wrinkles in the solar EUV illumination profile could manifest themselves in the TECP values. The effects of inhomogeneity and kinks/wrinkles in the solar EUV illumination profile during solar eclipse had been previously discussed in Mrak et al. (2018). Nevertheless, inhomogeneity in the solar EUV illumination profile may not always fully manifest itself in the TEC patterns. Here we discuss several aspects of the TEC data that are pertinent to the potential role(s) of inhomogeneous solar EUV illumination profile during this eclipse event.

Predominately, we direct our attention to a momentary increase (of ~ 10 min duration) in the solar EUV illumination around the maximum phase of the solar eclipse (cf. Fig. 4b). The appearance of this brief yet distinct peak in the solar EUV illumination profile near the maximum eclipse phase probably arose due to the fact that it was an annular solar eclipse. In an annular solar eclipse, significant solar illumination would be present during the maximum eclipse phase with the rim of the solar disk left unobscured. Such an illumination by the rim of the solar disk would not be as prominent for a total solar eclipse. Despite the distinguishing form of this mini-climax in EUV illumination, there was no corresponding bump in the TEC or ΔTEC values in response to it. The TEC or ΔTEC data had been gridded with 3 min time resolution, which should provide sufficient sampling to capture such a bump in TEC or ΔTEC had it actually existed. Most likely, the duration of exposure was too short for the TEC to respond in ways that would closely mimic the aforementioned mini climax.

The next set of aspects to be discussed is associated with the TECP values. Fluctuation patterns in TECP values that correlate with the eclipse events along the parallel evaluation arc and the four x-cut lines can be seen in Figs. 12 and 15. Fluctuations in TECP values can be associated with TIDs that are driven by AGWs in the neutral part of the upper atmosphere. However, it is also possible that fluctuation patterns in TECP values were due to modulation by kinks/wrinkles in the solar EUV illumination profile. Fluctuation patterns in TECP due to these two factors will have different characteristic properties. If the TECP fluctuation originated from solar EUV modulation, the resultant TECP fluctuation patterns should have a high degree of similarity to patterns that are visible in the calculated Laplacian EUV profile (cf. Figs. 17 and 18).

The calculated Laplacian EUV profile in Fig. 17 showed a prominent feature around the maximum eclipse phase. This feature was oriented in parallel to the C1/max/C4 epoch lines that ran from west to east. When compared with the TECP data (cf. the third column of Fig. 12), there were similar features that also appeared along the maximum eclipse epoch line. In this aspect, there is a notable similarity between the Laplacian EUV pattern and the observed TECP pattern. Likewise, the TECP data in Fig. 15 show a number of stripes that are well aligned with their respective C1/max/C4 epoch lines, matching the general orientation of the surface texture of the Laplacian EUV pattern shown in Fig. 18. These characteristics are consistent with fluctuations due to direct modulation by inhomogeneous solar EUV illumination.

However, there were other features that differ significantly between the Laplacian EUV pattern and the TECP observations. The surface texture of the Laplacian EUV in Fig. 17 ran generally parallel to the C1/max/C4 epoch lines. Meanwhile, in the TECP data (cf. Fig. 12a.iii and b.iii), there are fluctuation patterns between longitudes 92 and 102° E around 06:00 UTC, with wavefronts that are oriented sideways, deviating considerably from the orientation of the C1/max/C4 epoch lines. In addition, the large bulge in TECP that appeared between C1 and the maximum eclipse along x-cut no. 3 (cf. Fig. 15b) were not predicted by the Laplacian EUV calculation (cf. Fig. 18c). This TECP feature is more consistent with AGW/TID. Further, there was a special feature in the Laplacian EUV pattern (cf. Fig. 18, all panels), where pairs of pod-shaped blobs appeared around the moment of maximum eclipse, sandwiching the annularity region. This particular pattern was present in the calculated Laplacian EUV profile for all x-cut lines and hence is not an isolated incidence. However, no associated feature was found in the TECP data. The absence of the sandwich feature in the TECP data reveals some limitations in how much the inhomogeneous solar EUV illumination can directly modulate the ionosphere. Our findings on emergent features of wavelike perturbations in TEC data during the 26 December 2019 eclipse are consistent with Barad et al. (2022), who found similar features from observations over the Indian region, while ours came from the Southeast Asian region and specifically the Indonesian sector.

5 Summary and conclusion

We have examined a number of ionospheric effects associated with the passage of an annular solar eclipse on 26 December 2019 over the Indonesian region. Observation data from ionosonde and ground-based GPS receiver instruments, accompanied by solar-imagery data from the SDO AIA instrument, were analyzed in the study. The conclusions are as follows.

1. Ionosonde observations indicate reduction and subsequent recovery of ionospheric density during the solar eclipse, with the rates of reduction/recovery not necessarily symmetrical. The relative reductions of *fo*F2 and *fo*F1 were in the ranges of 24.0 %–27.5 % and 27 %–33 %, respectively. The rates of electron density reduction and recovery in the F2 layer were in the ranges of 20.6–43.0 el cm^{-3} s^{-1} (0.51–1.03 MHz h^{-1} in terms *fo*F2) and 19.9–23.0 el cm^{-3} s^{-1} (0.48–0.53 MHz h^{-1} in terms of *fo*F2), respectively.

2. Ionosonde observations indicate a delay between maximum eclipse and minimum *fo*F2 (considerable time delay between 34 and 36 min) and between maximum eclipse and minimum *fo*F1 (much shorter time delay between 9 and 16 min).

3. Ionosonde observations indicate that *hp*F2 descended (by 50–136 km) at the start of the eclipse. During the latter half of the eclipse, *hp*F2 was seen rising to reach 682–747 km (220–326 km higher than the normal baseline). The apparent *hp*F2 rise started to happen ∼ 11 min after the maximum eclipse and ended ∼ 90 min after the maximum eclipse.

4. Relative TEC reduction around the eclipse trajectory was in the 24.9 %–28.5 % range. We found an interesting feature where the greatest TEC reduction occurred to the north of the eclipse trajectory, even though the lunar shadow came at an angle from the south. It was probably facilitated by the equatorial fountain effect, which helped siphon plasma from the geomagnetic equator (north of the eclipse path) and transport it toward the ±15° MLAT area.

5. During the eclipse, wavelike fluctuations in the TECP data were found. Mechanisms associated with AGW/TID and direct modulation by nonuniform solar EUV illumination, each with its own characteristics, were considered. Some features in the TECP are characteristically more consistent with AGW/TID, while other features could be compatible with the solar EUV modulation effect based on analysis of SDO AIA solar images. However, a set of distinct solar EUV modulation patterns that had been predicted in the solar image analysis failed to manifest in TECP observations. This may indicate that the ability of nonuniform solar EUV illumination to modulate ionospheric plasma density configuration is highly sensitive to the particulars of the solar-eclipse event.

Data availability. Scaled ionogram parameters and processed GPS TEC data used in this study as well as supplementary figures and tables are made available via https://doi.org/10.7910/DVN/ZUXCCK (Harjosuwito, 2022).

Video supplement. An animated sequence of solar AIA images with synthetic lunar disk masking, an animated sequence of data maps showing spatiotemporal evolution GPS TEC values on individual IPPs at 350 km altitude, and an animated sequence of data maps showing the spatiotemporal evolution of the Laplacian of solar EUV irradiance over the studied region can be accessed via https://doi.org/10.7910/DVN/ZUXCCK (Harjosuwito, 2022).

Supplement. The supplement related to this article is available online at: https://doi.org/10.5194/angeo-41-147-2023-supplement.

Author contributions. Conceptualization: JH, VD, AH, JM, AF, RP. Ionosonde data acquisition: AB, E. Ionosonde data processing and analysis: JH, VD, AF, RP. GPS data curation: AH, AS. GPS

data processing and analysis: RP, AH. Solar EUV image data curation and analysis software development: JM. Methodology formulation: RP, JH. Supervision: RP. Manuscript writing – original draft: JH, VD, AH, JM, AF, RP. Manuscript editing: RP, VD.

Competing interests. The contact author has declared that none of the authors has any competing interests.

Disclaimer. Publisher's note: Copernicus Publications remains neutral with regard to jurisdictional claims in published maps and institutional affiliations.

Acknowledgements. The authors thank the technical staff and ionosonde operators at BPAA LAPAN Pontianak and Agam (Kototabang) and the BIG INACORS network for maintaining and operating the research equipment. The authors also thank Ecep Edi Hidayat for his help in manual scaling of raw ionogram data. The Dst index data can be accessed at https://wdc.kugi.kyoto-u.ac.jp/dstdir/ (last access: 4 April 2023). The Kp index data can be accessed at https://kp.gfz-potsdam.de/en (last access: 4 April 2023). The F10.7 index data can be accessed at https://omniweb.gsfc.nasa.gov/form/dx1.html (last access: 4 April 2023). The AIA SDO image data can be accessed at https://sdo.gsfc.nasa.gov/data/aiahmi/ (last access: 4 April 2023). Information on the BIG INACORS network can be found at http://inacors.big.go.id/sbc/ (last access: 4 April 2023).

Financial support. Rezy Pradipta's time was partially supported by AFOSR grant FA9550-20-1-0313.

Review statement. This paper was edited by Igo Paulino and reviewed by two anonymous referees.

References

Aa, E., Zhang, S.-R., Erickson, P. J., Goncharenko, L. P., Coster, A. J., Jonah, O. F., Lei, J., Huang, F., Dang, T., and Liu, L.: Coordinated ground-based and space-borne observations of ionospheric response to the annular solar eclipse on 26 December 2019, J. Geophys. Res.-Space, 125, e2020JA028296, https://doi.org/10.1029/2020JA028296, 2020.

Adekoya, B. and Chukwuma, V.: A Study of the Response of the Mid-Latitude Ionospheric f2 to the Total Solar Eclipses of Solar Cycle 23, Indian J. Radio Space, 41, 594–605, http://nopr.niscpr.res.in/handle/123456789/15634 (last access: 4 April 2023), 2012.

Adekoya, B. J., Chukwuma, V. U., and Reinisch, B. W.: Ionospheric vertical plasma drift and electron density response during total solar eclipses at equatorial/low latitude, J. Geophys. Res.-Space, 120, 8066–8084, https://doi.org/10.1002/2015JA021557, 2015.

Adekoya, B. J., Adebesin, B. O., David, T. W., Ikubanni, S. O., Adebiyi, S. J., Bolaji, O. S., and Chukwuma, V. U.: Solar-eclipse-induced perturbations at mid-latitude during the 21 August 2017 event, Ann. Geophys., 37, 171–182, https://doi.org/10.5194/angeo-37-171-2019, 2019.

Adeniyi, J. O., Radicella, S. M., Adimula, I. A., Willoughby, A. A., Oladipo, O. A., and Olawepo, O.: Signature of the 29 March 2006 eclipse on the ionosphere over an equatorial station, J. Geophys. Res., 112, A06314, https://doi.org/10.1029/2006JA012197, 2007.

Adeniyi, J. O., Oladipo, O. A., Radicella, S. M., Adimula, I. A., and Olawepo, A. O.: Analysis on 29 March 2006 eclipse effect on the ionosphere over Ilorin, Nigeria, J. Geophys. Res.-Space, 114, A11303, https://doi.org/10.1029/2009JA014416, 2009.

Afraimovich, E. L., Kosogorov, E. A., and Lesyuta, O. S.: Effects of the August 11, 1999 total solar eclipse as deduced from total electron content measurements at the GPS network, J. Atmos. Sol.-Terr. Phy., 64, 1933–1941, https://doi.org/10.1016/S1364-6826(02)00221-3, 2002.

Anastassiades, M. (Ed.): The annular solar eclipse on May 20, 1966 and the ionosphere, in: Solar Eclipses and the Ionosphere, Springer, Boston, MA, 253–271, https://doi.org/10.1007/978-1-4684-1839-2_16, 1970.

Anastassiades, M. and Moraitis, G.: On the behavior of *fo*F2 during the 20 May 1966 solar eclipse, J. Atmos. Terr. Phys., 30, 1471–1478, https://doi.org/10.1016/S0021-9169(68)90191-8, 1968.

Anggarani, S., Harjosuwito, J., Husin, A., Dear, V., and Ekawati, S.: Changes of *Nm*F2 and *hm*F2 over Biak (1° S, 136° E) during total solar eclipse on March 9, 2016, J. Phys. Conf. Ser., 771, 012037, https://doi.org/10.1088/1742-6596/771/1/012037, 2016.

Aplin, K. L., Scott, C. J., and Gray, S. L.: Atmospheric changes from solar eclipses, Philos. T. R. Soc. A, 374, 20150217, https://doi.org/10.1098/rsta.2015.0217, 2016.

Aryal, S., Evans, J. S., Correira, J., Burns, A. G., Wang, W., Solomon, S. C., Laskar, F. I., McClintock, W. E., Eastes, R. W., Dang, T., Lei, J., Liu, H., and Jee, G.: First global-scale synoptic imaging of solar eclipse effects in the thermosphere, J. Geophys. Res.-Space, 125, e2020JA027789, https://doi.org/10.1029/2020JA027789, 2020.

Atulkar, R., Khan, P. A., Jeevakhan, H., and Purohit, P. K.: Ionospheric response to annular and partial solar eclipse of 29 April 2014 in Antarctica and Australian Regions, Russian Journal of Earth Sciences, 15, ES2002, https://doi.org/10.2205/2015ES000549, 2015.

Bamford, R. A.: The effect of the 1999 total solar eclipse on the ionosphere, Phys. Chem. Earth Pt. C, 26, 373–377, https://doi.org/10.1016/S1464-1917(01)00016-2, 2001.

Barad, R. K., Sripathi, S., and England, S. L.: Multi-instrument observations of the ionospheric response to the 26 December 2019 solar eclipse over Indian and Southeast Asian longitudes, J. Geophys. Res.-Space, 127, e2022JA030330, https://doi.org/10.1029/2022JA030330, 2022.

Beynon, W. J. G.: Solar eclipses and the ionosphere, Nature, 176, 947–948, https://doi.org/10.1038/176947a0, 1955.

Birt, W. R.: Meteorological observations made during the solar eclipse of May 15, 1836, at Greenwich, The London, Edinburgh, and Dublin Philosophical Magazine and Journal of Science, 9, 393–394, https://doi.org/10.1080/14786443608649024, 1836.

Bravo, M., Martinez-Ledesma, M., Foppiano, A., Urra, B., Ovalle, E., Villalobos, C., Souza, J., Carrasco, E., Muñoz, P. R., Tamblay, L., Vega-Jorquera, P., Marín, J., Pacheco, R., Rojo, E., Leiva, R., and Stepanova, M.: First report of an eclipse from Chilean

ionosonde observations: Comparison with total electron content estimations and the modeled maximum electron concentration and its height, J. Geophys. Res.-Space, 125, e2020JA027923, https://doi.org/10.1029/2020JA027923, 2020.

Burton, E. T. and Boardman, E. M.: Effects of solar eclipse on audio frequency atmospherics, Nature, 131, 81–82, https://doi.org/10.1038/131081a0, 1933.

Chen, G., Zhao, Z., Ning, B., Deng, Z., Yang, G., Zhou, C., Yao, M., Li, S., and Li, N.: Latitudinal dependence of the ionospheric response to solar eclipse of 15 January 2010, J. Geophys. Res., 116, A06301, https://doi.org/10.1029/2010JA016305, 2011.

Chen, G., Qi, H., Ning, B., Zhao, Z., Yao, M., Deng, Z., Li, T., Huang, S., Feng, W., Wu, J., and Wu, C.: Nighttime ionospheric enhancements induced by the occurrence of an evening solar eclipse, J. Geophys. Res.-Space, 118, 6588–6596, 2013.

Cheng, K., Huang, Y.-N., and Chen, S.-W.: Ionospheric effects of the solar eclipse of September 23, 1987, around the equatorial anomaly crest region, J. Geophys. Res., 97, 103–111, https://doi.org/10.1029/91JA02409, 1992.

Cherniak, I. and Zakharenkova, I.: Ionospheric total electron content response to the great American solar eclipse of 21 August 2017, Geophys. Res. Lett., 45, 1199–1208, https://doi.org/10.1002/2017GL075989, 2018.

Choudhary, R. K., St.-Maurice, J.-P., Ambili, K. M., Sunda, S., and Pathan, B. M.: The impact of the January 15, 2010, annular solar eclipse on the equatorial and low latitude ionospheric densities, J. Geophys. Res., 116, A09309, https://doi.org/10.1029/2011JA016504, 2011.

Chukwuma, V. U. and Adekoya, B. J.: The effects of March 20 2015 solar eclipse on the F2 layer in the mid-latitude, Adv. Space Res., 58, 1720–1731, https://doi.org/10.1016/j.asr.2016.06.038, 2016.

Chuo, Y. J.: Ionospheric effects on the F region during the sunrise for the annular solar eclipse over Taiwan on 21 May 2012, Ann. Geophys., 31, 1891–1898, https://doi.org/10.5194/angeo-31-1891-2013, 2013.

Coster, A. J., Gaposchkin, E. M., and Thornton, L. E.: Real-time ionospheric monitoring system using GPS, Navigation, 39, 191–204, https://doi.org/10.1002/j.2161-4296.1992.tb01874.x, 1992.

Coster, A. J., Goncharenko, L., Zhang, S. R., Erickson, P. J., Rideout, W., and Vierinen, J.: GNSS observations of ionospheric variations during the 21 August 2017 solar eclipse, Geophys. Res. Lett., 44, 12041–12048, 2017.

Dear, V. and Yulianto, R.: Skywave propagation analysis during solar eclipse on 9 March 2016, Jurnal Sains Dirgantara, 14, 43–56, 2016.

Dear, V., Husin, A., Anggarani, S., Harjosuwito, J., and Pradipta, R.: Ionospheric effects during the total solar eclipse over Southeast Asia-Pacific on 9 March 2016: Part 1. Vertical movement of plasma layer and reduction in electron plasma density, J. Geophys. Res.-Space, 125, e2019JA026708, https://doi.org/10.1029/2019JA026708, 2020.

Eastes, R. W., McClintock, W. E., Codrescu, M. V., Aksnes, A., Anderson, D., Andersson L., Baker, N., Burns, A. G., Budzien, S. A., Daniell, R. E., Dymond, K. F., Eparvier, F. G., Harvey, J. E., Immel, T. J., Krywonos, A., Lankton, M. R., Lumpe, J. D., Prölss, G. W., Richmond, A. D., Rusch, D. W., Siegmund, O. H., Solomon, S. C., Strickland, D. J. and Woods, T. N.: Global-scale Observations of the Limb and Disk (GOLD): new observing capabilities for the ionosphere-thermosphere, Midlatitude Ionospheric Dynamics and Disturbances, Geophys. Monogr. Ser., 181, 319–326, 2008.

Eather, R. H., Mende, S. B., and Judge, R. J. R.: Plasma injection at synchronous orbit and spatial and temporal auroral morphology, J. Geophys. Res., 81, 2805–2824, 1976.

Espenak, F.: Annular Solar Eclipse of 2019 December 26, Eclipse Predictions by Fred Espenak, NASA Goddard Space Flight Center, https://eclipse.gsfc.nasa.gov/ (last access: 4 April 2023), 2019.

Evans, J. V.: An F-region eclipse, J. Geophys. Res., 70, 131–142, https://doi.org/10.1029/JZ070i001p00131, 1965.

Farges, T., Jodogne, J. C., Bamford, R., Le Roux, Y., Gauthier, F., Vila, P. M., Altadill, D., Sole, J. G., and Miro, G.: Disturbances of the western European ionosphere during the total solar eclipse of 11 August 1999 measured by a wide ionosonde and radar network, J. Atmos. Sol.-Terr. Phy., 63, 915–924, https://doi.org/10.1016/S1364-6826(00)00195-4, 2001.

Faturahman, A., Dear, V., Harjosuwito, J., Bahar, A., Husin, A., and Pradipta, R.: Ionospheric Observation Using Equatorial Atmosphere Radar (EAR) Kototabang for the 26 December 2019 Annular Solar Eclipse Research, in: Proceedings of the International Conference on Radioscience, Equatorial Atmospheric Science and Environment and Humanosphere Science, edited by: Yulihastin, E., Abadi, P., Sitompul, P., and Harjupa, W., Springer Proceedings in Physics, vol. 275, Springer, Singapore, https://doi.org/10.1007/978-981-19-0308-3_23, 2022a.

Faturahman, A., Harjosuwito, J., Afero, F., and Purwono, A.: Perubahan Lapisan F Ionosfer di Atas Pontianak pada Saat Gerhana Matahari Cincin 26 Desember 2019, Jurnal Sains Dirgantara, 19, 41–52, 2022b (in Indonesian).

Frissell, N. A., Katz, J. D., Gunning, S. W., Vega, J. S., Gerrard, A. J., Earle, G. D., Moses, M. L., West, M. L., Huba, J. D., Erickson, P. J., Miller, E. S., Gerzoff, R. B., Liles, W., and Silver, H. W.: Modeling amateur radio soundings of the ionospheric response to the 2017 great American eclipse, Geophys. Res. Lett., 45, 4665–4674, https://doi.org/10.1029/2018GL077324, 2018.

Fukao, S., Hashiguchi, H., Yamamoto, M., Tsuda, T., Nakamura, T., Yamamoto, M. K., Sato, T., Hagio, M., and Yabugaki, Y.: Equatorial Atmosphere Radar (EAR): System description and first results, Radio Sci., 38, 1053, https://doi.org/10.1029/2002RS002767, 2003.

Gage, K. S., Ecklund, W. L., Balsley, B. B., Soegijo, J., Pardede, M., and Notosuyidno, S. M.: A proposed ST radar for Biak, Indonesia (1° S, 136° E), in: Middle Atmosphere Program: Handbook for MAP, vol. 28, Extended Abstracts Fourth Workshop on Technical and Scientific Aspects of MST Radar Kyoto, 28 November–2 December 1988, Kyoto, edited by: Liu, C. H. and Edwards, B., p. 516, 1989.

Gledhill, J. A.: The effects of a solar eclipse on a stratified ionosphere, J. Atmos. Sol.-Terr. Phy., 16, 360–366, 1959.

Goncharenko, L. P., Erickson, P. J., Zhang, S.-R., Galkin, I., Coster, A. J., and Jonah, O. F.: Ionospheric response to the solar eclipse of 21 August 2017 in Millstone Hill (42N) observations, Geophys. Res. Lett., 45, 4601–4609, https://doi.org/10.1029/2018GL077334, 2018.

Gonzalez, R. C. and Woods, R. E.: Digital Image Processing, 4th edn., Pearson, New York, ISBN 10: 1-292-22304-9, 2018.

Gordon, W. E.: Arecibo ionospheric observatory: Studies of the upper atmosphere and planets are made with the aid

of a huge reflector in Puerto Rico, Science, 146, 26–30, https://doi.org/10.1126/science.146.3640.26, 1964.

Haggard, R.: Ionospheric Station Information Bulletin no. 46, Ionospheric Network Advisory Group (INAG), August 1985, https://www.sws.bom.gov.au/IPSHosted/INAG/ (last access: 4 April 2023), 1985.

Haggard, R.: Ionospheric Station Information Bulletin no. 51, Ionospheric Network Advisory Group (INAG), February 1988, https://www.sws.bom.gov.au/IPSHosted/INAG/ (last access: 4 April 2023), 1988.

Hairston, M. R., Mrak, S., Coley, W. R., Burrell, A., Holt, B., Perdue, M., Depew, M., and Power, R.: Topside ionospheric electron temperature observations of the 21 August 2017 eclipse by DMSP spacecraft, Geophys. Res. Lett., 45, 7242–7247, https://doi.org/10.1029/2018GL077381, 2018.

Hanuise, C., Broche, P., and Ogubazghi, G.: HF Doppler observations of gravity waves during the 16 February 1980 solar eclipse, J. Atmos. Sol.-Terr. Phy., 44, 963–966, 1982.

Harding, B. J., Drob, D. P., Buriti, R. A., and Makela, J. J.: Nightside detection of a large-scale thermospheric wave generated by a solar eclipse, Geophys. Res. Lett., 45, 3366–3373, https://doi.org/10.1002/2018GL077015, 2018.

Hargreaves, J. K.: The Solar-Terrestrial Environment: An Introduction to Geospace – the Science of the Terrestrial Upper Atmosphere, Ionosphere, and Magnetosphere, Cambridge Atmospheric and Space Science Series, Cambridge University Press, New York, https://doi.org/10.1017/CBO9780511628924, 1992.

Harjosuwito, J.: Masked Solar Images and 2-D Regional GPS TEC Maps, Harvard Dataverse [data set, video], https://doi.org/10.7910/DVN/ZUXCCK, 2022.

Huba, J. D. and Drob, D.: SAMI3 prediction of the impact of the 21 August 2017 total solar eclipse on the ionosphere/-plasmasphere system, Geophys. Res. Lett., 44, 5928–5935, https://doi.org/10.1002/2017GL073549, 2017.

Jakowski, N., Stankov, S. M., Wilken, V., Borries, C., Altadill, D., Chum, J., Buresova, D., Boska, J., Sauli, P., Hruska, F., and Cander, Lj. R.: Ionospheric behavior over Europe during the solar eclipse of 3 October 2005, J. Atmos. Sol.-Terr. Phy., 70, 836–853, https://doi.org/10.1016/j.jastp.2007.02.016, 2008.

Jonah, O. F., Goncharenko, L., Erickson, P. J., Zhang, S., Coster, A., Chau, J. L., de Paula, E. R., and Rideout, W.: Anomalous behavior of the equatorial ionization anomaly during the 2 July 2019 solar eclipse, J. Geophys. Res.-Space, 125, e2020JA027909, https://doi.org/10.1029/2020JA027909, 2020.

Jose, L., Vineeth, C., Pant, T. K., and Kumar, K. K.: Response of the equatorial ionosphere to the annular solar eclipse of 15 January 2010, J. Geophys. Res.-Space, 125, e2019JA027348, https://doi.org/10.1029/2019JA027348, 2020.

Klobuchar, J. A.: Ionospheric Effects on GPS, in Global Positioning System: Theory and Applications, Vol. 1, edited by: Parkinson, B. W. and Spilker, J. J., American Institute of Aeronautics and Astronautics, Washington, 485–515, https://doi.org/10.2514/5.9781600866388.0485.0515, 1996.

Kumar, S., Singh, A. K., and Singh, R. P.: Ionospheric response to total solar eclipse of 22 July 2009 in different Indian regions, Ann. Geophys., 31, 1549–1558, https://doi.org/10.5194/angeo-31-1549-2013, 2013.

Kurkin, V. I., Nosov, V. E., Potekhin, V. F., Smirnov, V. F., and Zherebtsov, G. A.: The March 9, 1997 solar eclipse ionospheric effects over the Russian region, Adv. Space Res., 27, 1437–1440, https://doi.org/10.1016/S0273-1177(01)00030-8, 2001.

Le, H., Liu, L., Yue, X., Wan, W., and Ning, B.: Latitudinal dependence of the ionospheric response to solar eclipses, J. Geophys. Res., 114, A07308, https://doi.org/10.1029/2009JA014072, 2009.

Lerfald, G. M., Hargreaves, J. K., and Watts, J. M.: D-region absorption at 10 and 15 mc s^{-1} during the total solar eclipse of July 20, 1963, Radio Sci., 69D, 939–946, 1965.

Liu, J. Y., Yang, S. S., Rajesh, P. K., Sun, Y. Y., Chum, J., Pan, C. J., Chu, Y. H., Chao, C. K., and Chang, L. C.: Ionospheric response to the 21 May 2012 annular solar eclipse over Taiwan, J. Geophys. Res.-Space, 124, 3623–3636, https://doi.org/10.1029/2018JA025928, 2019.

Lynn, K. J. W., Harris, T. J., and Sjarifudin, M.: Stratification of the F2 layer observed in Southeast Asia, J. Geophys. Res.-Space, 105, 27147–27156, 2000.

Lynn, K. J. W., Sjarifudin, M., Harris, T. J., and Le Huy, M.: Combined TOPEX/Poseidon TEC and ionosonde observations of negative low-latitude ionospheric storms, Ann. Geophys., 22, 2837–2847, https://doi.org/10.5194/angeo-22-2837-2004, 2004.

Mansoori, A. A., Parvaiz, A., Khan, P. A., Bhawre, P., Purohit, P. K., and Gwal, A. K.: Solar eclipses and ionospheric effects: Some historical perspectives, International Journal of Geomatics and Geosciences, 1, 662–668, 2011.

Mannucci, A. J., Wilson, B. D., and Edwards, C. D.: A new method for monitoring the earth's ionospheric total electron content using the GPS global network, Proc. of ION GPS-93, Inst. of Navigation, 22–24 September 1993, Salt Lake City, UT, 1323–1332, 1993.

Masykur, M.: Analysis of accuracy the InaCORS BIG online post-processing service, Appl. Geomat., 13, 227–233, https://doi.org/10.1007/s12518-020-00343-2, 2021.

Minnis, C. M.: Ionospheric changes at Singapore during the solar eclipse of 20 June 1955, J. Atmos. Terr. Phys., 10, 229–236, 1957.

Mitra, S. K., Rakshit, H., Syam, P., and Ghose, B. N.: Effect of the solar eclipse on the ionosphere, Nature, 132, 442–443, https://doi.org/10.1038/132442a0, 1933.

Mrak, S., Semeter, J. L., Drob, D., and Huba, J. D.: Direct EUV/X-ray modulation of the ionosphere during the August 2017 total solar eclipse, Geophys. Res. Lett., 45, 3820–3828, https://doi.org/10.1029/2017GL076771, 2018.

Muslim, B., Sunardi, B., Merdijanto, U., Heryanto, D. T., Efendi, J., and Andrian, Y.: Ionospheric response to march 9th 2016 solar eclipse from palu gps data, Jurnal Meteorologi dan Geofisika, 17, 191–198, 2016.

Nixon, M. S. and Aguado, A. S.: Feature Extraction and Image Processing, 1st edn., Newnes, Oxford, ISBN 0-7506-5078-8, 2002.

Osborne, B. W.: Ionospheric behaviour in the F2 region at Singapore, J. Atmos. Terr. Phys., 2, 66–78, 1951.

Paulino, I., Figueiredo, C. A. O. B., Rodrigues, F. S., Buriti, R. A., Wrasse, C. M., Paulino, A. R., Barros, D., Takahashi, H., Batista, I. S., Medeiros, A. F., Batista, P. P., Abdu, M. A., de Paula, E. R., Denardini, C. M., Lima, L. M., Cueva, R. Y. C., and Makela, J. J.: Atmospheric gravity waves observed in the nightglow following the 21 August 2017 total solar eclipse, Geophys. Res. Lett., 47, e2020GL088924, https://doi.org/10.1029/2020GL088924, 2020.

Perkins, F. W., Salpeter, E. E., and Yngvesson, K. O.: Incoherent scatter from plasma oscillations in the ionosphere, Phys. Rev. Lett., 14, 579, 1965.

Perwitasari, S. and Muslim, B.: Respon ionosfer terhadap gerhana matahari 26 Januari 2009 dari pengamatan ionosonda, in: Prosiding Seminar Nasional Penelitian, Pendidikan, dan Penerapan MIPA, Fakultas MIPA, Universitas Negeri Yogyakarta, 16 May 2009, https://eprints.uny.ac.id/12313/ (last access: 4 April 2023), 2009 (in Indonesian).

Piggott, W. R. and Rawer, K.: URSI Handbook of Ionogram Interpretation and Reduction, 2nd Edn., Rep. UAG-23A, Nat. Oceanic and Atmos. Admin., U.S. Dep. of Comm., Washington, D.C., https://repository.library.noaa.gov/view/noaa/10404 (last access: 4 April 2023), 1972.

Pradipta, R., Valladares, C. E., and Doherty, P. H.: GPS observation of continent-size traveling TEC pulsations at the start of geomagnetic storms, J. Geophys. Res.-Space, 119, 6913–6924, https://doi.org/10.1002/2014JA020177, 2014.

Price, W. L.: Anomalous ionospheric reflection during solar eclipses, J. Atmos. Sol.-Terr. Phy., 16, 93–98, 1959.

Rama Rao, P. V. S., Gopi Krishna, S., Niranjan, K., and Prasad, D. S. V. V. D.: Temporal and spatial variations in TEC using simultaneous measurements from the Indian GPS network of receivers during the low solar activity period of 2004–2005, Ann. Geophys., 24, 3279–3292, https://doi.org/10.5194/angeo-24-3279-2006, 2006.

Ratcliffe, J. A.: A survey of solar eclipses and the ionosphere, in: Solar eclipses and the ionosphere, edited by: Beynon, W. J. G. and Brown, M. G., Pergamon Press, Oxford, 1–13, ISBN 9780080090467, 1956.

Resende, L. C. A., Zhu, Y., Denardini, C. M., Chen, S. S., Chagas, R. A. J., Da Silva, L. A., Carmo, C. S., Moro, J., Barros, D., Nogueira, P. A. B., Marchezi, J. P., Picanço, G. A. S., Jauer, P., Silva, R. P., Silva, D., Carrasco, J. A., Wang, C., and Liu, Z.: A multi-instrumental and modeling analysis of the ionospheric responses to the solar eclipse on 14 December 2020 over the Brazilian region, Ann. Geophys., 40, 191–203, https://doi.org/10.5194/angeo-40-191-2022, 2022.

Rideout, W. and Coster, A.: Automated GPS processing for global total electron content data, GPS Solut., 10, 219–228, https://doi.org/10.1007/s10291-006-0029-5, 2006.

Rishbeth, H.: Further analogue studies of the ionospheric F layer, Proc. Phys. Soc., 81, 65–77, 1963.

Rishbeth, H.: Solar eclipses and ionospheric theory, Space Sci. Rev., 8, 543–554, https://doi.org/10.1007/BF00175006, 1968.

Rishbeth, H. and Garriott, O. K.: Introduction to the Ionosphere and Geomagnetism, Stanford Electronics Laboratories, Stanford University, https://ntrs.nasa.gov/api/citations/19650007912/downloads/19650007912.pdf (last access: 4 April 2023), 1964.

Rishbeth, H. and Garriott, O. K.: Introduction to Ionospheric Physics, International Geophysics Series, vol. 14, Academic Press, New York, https://doi.org/10.1016/S0074-6142(09)60018-8, 1969.

Seemala, G. K. and Valladares, C. E.: Statistics of total electron content depletions observed over the South American continent for the year 2008, Radio Sci., 46, RS5019, https://doi.org/10.1029/2011RS004722, 2011.

Sen, H. Y.: Stratification of the F2-layer of the ionosphere over Singapore, J. Geophys. Res., 54, 363–366, 1949.

Setty, C. S. G. K.: Eclipse effects on the F-layer at sunrise, J. Atmos. Sol.-Terr. Phy., 19, 73–81, 1960.

Skone, S.: Wide area ionosphere grid modeling in the auroral region, PhD thesis, University of Calgary, Canada, 198 pp., https://prism.ucalgary.ca/items/b3c87036-bbbc-40e7-8a30-a5f4a0a1767f (last access: 4 April 2023), 1998.

Sridharan, R., Devasia, C. V., Jyoti, N., Tiwari, D., Viswanathan, K. S., and Subbarao, K. S. V.: Effects of solar eclipse on the electrodynamical processes of the equatorial ionosphere: a case study during 11 August 1999 dusk time total solar eclipse over India, Ann. Geophys., 20, 1977–1985, https://doi.org/10.5194/angeo-20-1977-2002, 2002.

St.-Maurice, J. P., Ambili, K. M., and Choudhary, R. K.: Local electrodynamics of a solar eclipse at the magnetic equator in the early afternoon hours, Geophys. Res. Lett., 38, L04102, https://doi.org/10.1029/2010GL046085, 2011.

Vita, A. N., Sunardi, B., Sulastri, and Sakya, A. E.: Pengaruh Gerhana Matahari 09 Maret 2016 Terhadap Kandungan Total Elektron Ionosfer, Prosiding Seminar Nasional Fisika, vol. VI, 51–56, https://doi.org/10.21009/03.SNF2017, 2017 (in Indonesian).

Wang, X.: Laplacian Operator-Based Edge Detectors, IEEE T. Pattern Anal., 29, 886–890, https://doi.org/10.1109/TPAMI.2007.1027, 2007.

Wang, X., Berthelier, J. J., and Lebreton, J. P.: Ionosphere variations at 700 km altitude observed by the DEMETER satellite during the 29 March 2006 solar eclipse, J. Geophys. Res., 115, A11312, https://doi.org/10.1029/2010JA015497, 2010.

Wang, Y., Zhang, Q. H., Ma, Y. Z., Jayachandran, P. T., Xing, Z. Y., Balan, N., and Zhang, S. R.: Polar ionospheric large-scale structures and dynamics revealed by TEC keogram extracted from TEC maps, J. Geophys. Res.-Space, 125, e2019JA027020, https://doi.org/10.1029/2019JA027020, 2020.

Zhang, S.-R., Erickson, P. J., Goncharenko, L. P., Coster, A. J., Rideout, W., and Vierinen, J.: Ionospheric bow waves and perturbations induced by the 21 August 2017 solar eclipse, Geophys. Res. Lett., 44, 12067–12073, https://doi.org/10.1002/2017GL076054, 2017.